LLNL-TR-851939

LAWRENCE
LIVERMORE
NATIONAL
LABORATORY

Adjoint Waveform Tomography for Crustal and Upper Mantle Structure the Middle East and Southwest Asia for Improved Waveform Simulations Using Openly Available Broadband Data

A. Rodgers

July 21, 2023

This work performed under the auspices of the U.S. Department of Energy by Lawrence Livermore National Laboratory under Contract DE-AC52-07NA27344.

Adjoint Waveform Tomography for Crustal and Upper Mantle Structure the Middle East and Southwest Asia for Improved Waveform Simulations Using Openly Available Broadband Data

Report to the National Nuclear Security Agency Ground-Based Nuclear Explosion Detection

For the FY2023 WAVEFORMS Project

Arthur J. Rodgers

Geophysical Monitoring Program, Lawrence Livermore National Laboratory,

Livermore, CA 94551 USA

July 27, 2023

Summary

We present a new model of radially anisotropic seismic wavespeeds for the crust and upper mantle of a broad region of the Middle East and Southwest Asia (MESWA) derived from adjoint waveform tomography. We inverted waveforms from 192 Global Centroid Moment Tensor earthquakes (M_W 5.5-7.0) recorded by over 1000 openly available broadband seismic stations from permanent and temporary networks in the region. Spatial coverage of the available data is highly uneven due to earthquakes clustered along plate boundaries and sparse coverage of open seismic networks in the region. We considered three possible starting models: the SPiRaL global model (Simmons et al., 2021); MEC-1 (Kaviani et al., 2020); and CSEM2.0 (Noe et al., 2023). Because the SPiRaL model provides good fits to the observed waveforms measured by the time-bandwidth product of selected windows in several period bands, provides all the necessary parameters and covers the entire domain we used it for the starting model with the period band 50-100 seconds. Inversion iterations proceeded using time-frequency phase misfits in six stages and 54 total iterations reducing the minimum period to 30 seconds. Our final model, MESWA, provides improved waveform fits compared to the starting model for both the data used in the inversion and an independent validation data set of 66 events. Two metrics of waveform fit (the time-frequency phase misfit used in the optimization and normalized L2 misfit) were both reduced by nearly 60% for both data sets and MESWA provides significantly larger misfit reductions relative to the SPiRaL model than the MEC-1 or CSEM models. We also find that MESWA provides a larger time-bandwidth product of selected windows indicating that more information content of the observed waveforms is explained by MESWA than the other models. Our new model reveals tectonic features imaged by other studies and methods but in a new holistic model of shear and compressional wavespeeds (v_S and v_P, respectively) with anisotropy covering the crust and uppermost mantle of a larger domain. MESWA has smaller scale-length features and tends to sharpen some features relative to the SPiRaL starting model. Examples include: low crustal v_S in the Turkish-Iranian Plateau, Zagros Mountains, Afghan Central Blocks and Sulaiman Fold Belt; low mantle v_S following divergent (Gulf of Aden, Red Sea) and transform (Dead Sea Fault) margins of the Arabian Plate; low and high v_S in the mantle beneath the Arabian Shield and Platform, respectively. Low v_S is imaged below Cenozoic volcanic centers of the Arabian Peninsula, the so-called Mecca-Madina-Nafud (MMN) Line. Positive anisotropy ($v_{SH} > v_{SV}$) is inferred for asthenospheric depths across the region except where up/downwelling may influence fabric alignment (e.g. Afar, Red Sea, Arabian Shield). Elevated v_S tracks Makran subduction under southeast Iran. MESWA resembles the SPiRaL model in its long-wavelength structure, but enhances shorter wavelengths features on the order of 200 km and smaller. The resulting model could be used for as a starting model for further improvements, say using waveforms from in-country seismic networks that are not openly available or smaller-scale studies targeting shorter period waveforms. The model also could be used for source characterization and moment tensor inversion to improve earthquake hazard studies and nuclear explosion monitoring.

Key Words: Tomography, Waveform inversion, Computational seismology, Middle East, Southwest Asia

Introduction

The Middle East and Southwest Asia (MESWA) is a geologically complex region including the interaction of several tectonic plates. Figure 1 shows the study region, which includes all of the Arabian Plate and parts of the Eurasian, African and Indian Plates. Plate boundaries include: continental transforms of the North Anatolian and Dead Sea Faults; continental convergence along the Turkish-Iranian Plateau, and Indian-Eurasian Collision (transpressional plate boundary along Afghanistan-Pakistan border, Sulaiman Fold Belt, Central Afghanistan Highlands, Hindu Kush, Pamirs); ocean spreading along the Red Sea, Gulf of Aden and Owen Fracture Zone; and subduction of oceanic lithosphere along the Makran north of the Gulf of Oman and Arabian Sea. Complex active tectonics of the region is revealed by abundant but uneven seismicity including large damaging earthquakes and volcanic activity. Figure 2 shows the events used for the model inversion and validation (discussed in detail below) and is representative of the seismicity in the region.

Parts of the region have been intensively studied tracking the deployment of seismic sensors, while other regions have been the subject of fewer investigations. Many of the detailed investigations of the region have benefited from access to closed (proprietary) data from networks operating in specific countries (Al-Lazki et al., 2004; Al-Damegh et al., 2005; Hansen et al., 2006; Hansen et al., 2007; Park et al., 2007; Park et al., 2008; Al-Lazki et al., 2014; Tang et al., 2019; Kaviani et al., 2020; Kim et al., 2023; Movaghari and Doloei, 2023). Structure of the crust and upper mantle has been revealed by seismic tomography using various methodologies and data sets. These include travel time tomography (Hearn and Ni, 1994; Al-

Lazki et al., 2003, 2004, 2014; Park et al., 2007), receiver functions (Al-Damegh et al., 2005; Hansen et al., 2006), earthquake and ambient noise surface wave dispersion (e.g. Mokhtar et al., 2001; Villasenor et al., 2001; Park et al., 2008; Kim et al. 2023), waveform inversion (Maggi and Priestley, 2005; Chang et al., 2010a) and joint inversions of different data sets (Julia et al., 2003; Tkalčić et al., 2005; Chang et al., 2010b; Tang et al., 2019; Kaviani et al., 2020; Movaghari and Doloei, 2020) with this list meant to be representative but not exhaustive.

This study reports a new model of radially anisotropic seismic wavespeeds for the MESWA region shown in Figure 1. The model is derived from adjoint waveform tomography using broadband seismic waveform data from only openly available sources through Federation of Digital Seismic Networks (FDSN) webservices. Several permanent seismic networks operate stations in the region, however those with global coverage and openly available data are sparse (e.g. IRIS-Ida, IRIS-USGS, Geofone, Geoscope). Regional networks in Turkey, Greece and Central Asia provide open data for clustered stations. Temporary networks have been deployed in specific areas for 1-2 year durations and these improve the coverage.

Adjoint waveform tomography is a waveform inversion methodology which uses the full three-dimensional (3D) sensitivity of observed seismograms to Earth structure (usual only seismic wavespeeds). The methodology is now widely used and is described in seminal studies (e.g., Tarantola, 1988, Tromp et al., 2005; Liu and Tromp, 2005; Fichtner et al, 2006, Tape et al., 2007) and reviews (e.g. Fichtner, 2010; Liu and Gu, 2012; Tromp, 2020). In this study, we closely followed the methodology of Rodgers et al. (2022) for the western United States. The resulting model provides improvement in quantitative measures of waveform misfit compared to the starting and other models and many known large-scale tectonic features are imaged. This study establishes a baseline of what features can be imaged with openly available sparse data for this large and tectonically complex continental-scale domain and will be useful to compare against other studies with data from national seismic networks that are not openly available.

This article is organized as follows. In the next section we describe the data selection and considerations for choosing a starting model. We follow this with a description of the adjoint waveform tomography methodology applied to the region and data set. We then describe the resulting model, demonstrate its efficacy for fitting observed waveforms and interpret the imaged features in terms of known tectonic processes. We conclude with a discussion of strategies for future improvements and recommendations.

Data Selection and Starting Model

We started by selecting earthquakes from the Global Centroid Moment Tensor (GCMT) catalog (Ekström et al., 2012) in the domain (Figure 1) with moment magnitude, M_W, between 5.5 and 7.0 for the time period 1995-2020. This resulted in 327 events. We then collected openly available broadband waveforms for these events that were recorded by permanent and temporary seismic station networks in the domain from Federation of Digital Seismic Network (FDSN) webservices using ObsPy (Krischer et al., 2015a). Based on the initial waveform fits (described below) and the number and spatial coverage of paths we selected 192 events for the inversion and 66 events for model validation (Figures 2a and 2b, respectively). These events were recorded by over 1000 stations in the domain. Figure 3 shows the broadband stations from permanent (over 300) and temporary (over 600) seismic networks used in the inversion. Openly available permanent networks (Figure 3a) cover the region are very sparsely. Permanent networks cover the Aegean Sea and Turkish Plateau (Greece and Turkey), Eastern Mediterranean Sea (Cyprus, Israel), the Caucasus (Armenia, Georgia) and the Hindu Kush, Pamir and Tien Shan (Kyrgyzstan, Tajikistan). Some whole countries are covered by no or only a few openly available permanent stations. Temporary networks (Figure 3b) provide about twice as many stations as the permanent networks although they are typically deployed for a short duration (e.g. 1-2 years). These stations provide complementary coverage in some regions poorly covered by permanent stations (e.g. Ethiopia, Eretria, Yemen, Oman, Saudi Arabia and Iran). A complete listing of events and seismic stations used in both the inversion and validation data sets is provided in Rodgers (2023).

Adjoint waveform tomography (AWT) requires complete waveform simulations in a three-dimensional (3D) seismic Earth model describing wavespeeds, density and attenuation. Measurements of differences between the observed waveforms and those simulated from the current model to compute sensitivity kernels for model updates. AWT uses a multiscale iterative inversion procedure (e.g. Bunks et al., 1995; Fichtner et al., 2009, 2013; Tape et al. 2010) to improve phase errors (e.g. cycle skipping) and avoid getting trapped in local minima. An essential step in AWT is identifying waveform segments ("windows") where observed and simulated waveforms are in reasonably good agreement with slowly varying phase delay (less than $\pi/2$). Sensitivity kernels are computed from waveform metrics based on these windows. A good starting model should generate simulated waveforms that that fit observed waveforms at many receivers (paths). Such a model should provide long durations of well-correlated observed and synthetic waveforms. Ideally, a starting model should provide good waveform fits, cover the central area and depth extent of the target domain and provide the necessary parameters (wavespeeds, density and attenuation). Radial anisotropy which is important to model the Love-Rayleigh discrepancy commonly observed in long-period (> 20 seconds) regional surface waves (e.g. Gaherty and Jordan, 1995).

Doody et al. (2023) showed that a conservative multiscale inversion approach can result in models that are robust to the choice of starting model. We closely follow that approach here. For this region we considered three possible starting models. The SPiRaL model (Simmons et al., 2021) is a global model based on travel times and surface wave dispersion. It includes radial anisotropy as vertically and horizontally polarized shear wavespeeds (v_{SV} and v_{SH}, respectively) and compressional wavespeeds (v_{PV} and v_{PH}, respectively). Density and attenuation quality factors were scaled from wavespeeds. This model conforms to the global crustal thickness model CRUST1.0 (Laske et al., 2013). Although this model is not based waveform simulations, it has been shown to produce good waveform fits in various regions (Simmons et al., 2021; Rodgers et al., 2022).

The Midd_East_Crust_1 (MEC-1) model (Kaviani et al., 2020) is a regional shear wavespeed, v_S, model covering the Middle East, Arabian Peninsula and the Eastern

Mediterranean. It is based on vertical component Rayleigh surface wave dispersion measurements from earthquakes and ambient noise cross-correlations. This model covers all but the northern and eastern ~5° of our target domain (Figure 1) and extends to 105 km depth. MEC-1 benefits from data from at least two major national seismic networks that are not openly available (International Institute of Earthquake Engineering and Seismology in Iran and the Saudi Geological Survey in Saudi Arabia). Because MEC-1 is based on vertical component Rayleigh wave data it constrains vertically polarized shear wavespeeds, v_{SV}, and unfortunately has no constraints on transversely polarized shear wavespeeds, v_{SH}, compressional wavespeeds, v_P, and density, ρ. Without constraints on anisotropy in MEC-1, we interpreted MEC-1 as an isotropic model. Compressional wavespeeds and density were scaled from v_S following Brocher (2005). The model was tapered (with a 2° taper width) into isotropic PREM (Dziewonski and Anderson, 1981) to span the computational domain (Figure 1a, inset).

The Collaborative Seismic Earth Model version 2.0 (CSEM, Noe et al. 2022) is a global model based on multiscale adjoint waveform tomography following the approach of Afanasiev et al. (2016) and Fichtner et al. (2018). This model spans our domain and depth range and includes all the necessary material properties including radial anisotropy, density and attenuation. It is based on several regional models that intersect our target domain and updates the global material properties by waveform inversion.

In order to objectively select a starting model, we computed the waveforms for the three models described above and all events and paths in the computational domain.

Waveform simulations relied on the Salvus spectral-element method (Afanasiev et al., 2019) and the Salvus waveform modeling and inversion package (mondaic.com). We considered five period bands with minimum periods of 50, 40, 30, 25 and 20 seconds and a maximum period of 100 seconds. All observed and simulated waveforms were compared to define time windows for adjoint sources and gradients similar to the FLEXWIN algorithm of Maggi et al. (2009). We used the data selection method of Krischer (2015b) following recent studies (Rodgers et al., 2022; Doody et al., 2023). The algorithm finds time windows where agreement in amplitude and phase is good enough so that misfit can be measured, adjoint sources defined and sensitivity kernels can be computed. Waveforms with noise, interfering events, incorrect instrument response or amplitude errors were rejected by the algorithm.

Using these data selections based on window picking, two subsets were created from all events: one for the inversions and another for validation of the resulting model. Initial analysis of the waveform fits (confirmed below) showed that the SPiRaL model performed better than the MEC-1 and CSEM models across the period bands considered. We then choose 192 events for the inversion using windows picked with the SPiRaL model in the period band 50-100 seconds that met two criteria: each event had at least 10 receivers with windows and half of the receivers that recorded the event had windows. These choices were made to select the most well recorded events that best cover the domain. Similar event lists were found with the other models, though fewer and/or shorter windows were picked. A validation data set was created with 66 events from the remaining events also requiring that windows were picked on least 10 receivers. The inversion and validation events are shown in map view in Figure 2 and these events span the domain with similar coverage.

We then used metrics of the resulting windows to evaluate model performance. Specifically, we measured the time-bandwidth product (TBP) of the picked windows as introduced in Rodgers et al. (2022). The TBP is proportional to the information content in the selected windows, hence the larger this number for a fixed data set the better a model is at explaining the observed seismograms. Figure 4 shows the TBP as a function of the minimum period for the three models considered and all 327 events. For a given model, the TBP generally increases as the minimum period decreases due to the increase in bandwidth and the consistency of waveform agreement. We see how the TBP for the SPiRaL and MEC-1 models closely track each other except for the shortest minimum period of 20 seconds and that the CSEM model has slightly lower TBP values compared to other models. We chose to use the SPiRaL model for our starting model based on the TBP performance and that it includes radial anisotropy and covers the entire target domain and depth range. Note that we also include the TBP for the resulting MESWA model after inversion iterations in Figure 4, which shows how our AWT approach results in a model that improves waveform fits over the starting model and will be discussed below. Note furthermore that the MESWA model provides good performance (large and increasing TBP) for periods shorter than the those used in the inversion (30 seconds).

Figure 5 shows the events, stations and path coverage of the inversion and validation data sets based on the windows selected from synthetics from the SPiRaL model in the period band 50-100 seconds. Although the validation data set has fewer paths (only about 25% of the inversion data set) the coverage is very similar.

Adjoint Waveform Tomography Methodology

We followed a multiscale approach (Bunks et al., 1995; Fichtner et al. 2013) similar to other AWT studies (e.g. Tape et al., 2009; Zhu et al. 2015; Wehner et al., 2021; Rodgers et al., 2022; Doody et al., 2023). We chose to start with the longest periods (50-100 seconds) in order to make adjustments to the large-scale structure including the deep structure sampled by long period surface waves. We then reduced the minimum period and relaxed the smoothing to increase sensitivity to finer-scale structure in six inversion stages. Within each inversion stage the time windows and smoothing parameters were fixed. Inversions relied on the L-BFGS algorithm (Nocedal and Wright, 2006; Kennett and Fichtner, 2021) which has been shown to improve convergence (Modrak and Tromp, 2016; Liu et al., 2022). More specifically, we ran a trust-region L-BFGS inversion algorithm including a smoothing operator based on the diffusion equation into the initial approximation of the Hessian (Bunks et al., 1995; Conn et al., 2000; Boehm et al., 2018). The diffusion equation is solved individually for all inversion parameters as an initial condition. Because seismic wavespeeds vary much more strongly with depth than laterally, isotropic smoothing can have the undesirable effect of smearing sensitivity across a broad depth range. The smoothing operator is designed to be anisotropic with shorter smoothing length in the radial direction, λ_r, than in the arc directions, λ_ϑ and λ_ϕ. The smoothing length is defined as a fraction of the local v_{SV} wavelength in spherical coordinates.

Within each stage we allowed the inversion to iterate until it converged by failing to further reduce the misfit or by the trust region shrinking to small values (indicating the descent direction is poorly determined). The final model which we refer to as MESWA was obtained as the seventh (7^{th}) and final iteration from the sixth (6^{th}) inversion stage. The inversion stages and various parameters described in this section are provided in Table 1.

Table 1. Parameters describing the six inversion stages used to develop MESWA. Receiver tapers follow Ruan et al. (2019) and additionally include minimum and maximum taper distances for receiver weighting. Source/receiver cutouts are given in km. Smoothing lengths (l_r l_q, l_f) are given in units of the local v_{SV} wavelength in spherical coordinate directions. The Region-of-Interest (ROI) depth is the shallowest depth for which model updates are included. “Iterations in stage” tabulates the total number of unique iterations for each stage.

Stage	**Period Band (sec)**	**Receiver Tapers (min/max, km)**	**Cutouts (source/receiver, km)**	**Smoothing lengths l_r l_q, l_φ**	**ROI Depth (km)**	**Iterations in stage**
0	50-100	180/400	250/50	0.2, 1.0, 1.0	25	7
1	50-100	180/400	250/50	0.2, 0.5, 0.5	20	10
2	40-100	150/300	220/40	0.2, 0.5, 0.5	20	9
3	40-100	150/300	220/40	0.2, 0.5, 0.5	10	11
4	30-100	100/225	160/30	0.2, 0.5, 0.5	10	11
5	30-100	100/225	160/0	0.2, 0.5, 0.5	0	7

The data set was updated by re-picking the time windows at the start of each inversion stage. This illustrated the improvement in the model by the general increase of the time duration (window length) of windows picked for each inversion stage and the TBP of selected time windows (Table 2).

Table 2. Window statistics for the 6 inversion stages described in Table1 and the text: n_rec is the number of receivers with windows; n_windows is the number of windows; window length is the total time duration of windows in days; and the time-bandwidth product of selected windows is in days-Hz.

	stage	n_rec	n_windows	window length (days)	time-bandwidth product (days-Hz)
0	stage 0	13713	34659	58.386877	0.681180
1	stage_1	14344	36893	65.010631	0.758457
2	stage_2	15041	50778	73.064618	1.217744
3	stage_3	15127	47673	71.732055	1.195534
4	stage_4	15715	59373	68.976879	1.724422
5	stage_5	15776	60930	73.138763	1.828469

Inversions solved for updates to the wavespeeds and density (v_{SV}, v_{SH}, v_{PV} and v_{PH} and ρ). The long periods waveforms considered here were dominated by surface waves. Rayleigh waves provided some sensitivity to compressional wavespeeds, but these wavespeeds and their anisotropy were likely poorly resolved, particularly without isolating P-waveforms over broad distances. While density can have an effect on waveforms (Płonka et al., 2016; Blom et al., 2017), our misfits were based on phase (arrival time) and were most sensitive to wavespeeds. Our analysis here is focused on imaging shear wavespeeds.

In this study, we used time-frequency phase misfit for the waveform misfit objective function (Fichtner et al., 2009, 2013; Fichtner, 2010; Krischer et al., 2015b; 2016). This method decomposes the observed and simulated waveforms into the time-frequency domain following Kristeková et al., (2006; 2009) where phase difference of different frequency components is measured. Time-frequency phase misfits have the advantage of tracking time-varying phase errors between the observed and synthetic waveforms that can occur in dispersed (e.g. surface waves) or interfering signals (e.g. triplicated arrivals, scattered waves). Sensitivity kernels based on these frequency-dependent misfits include information across the entire range of periods and wavelengths in the bandwidth considered. This misfit function is thus multiscale similar to other misfits such as generalized seismological data functionals (Gee and Jordan, 1992), multitaper (Tape et al., 2010) or exponentiated phase (Bozdağ et al., 2011).

Once the event sensitivity kernels were computed, gradients for the volumetric inversion for model wavespeed updates were computed. These include various manipulations to mitigate potential problems due to: the outsized influence of near-source and near-receiver structure; the uneven distribution of receivers recording each event; and smoothing of rapid spatial variations in the kernels. To mitigate the outsized influence of misfits at short epicentral distances from the event, we applied a tapered weight to the near-source receivers. The taper function has two values: a minimum distance within which receiver contributions to the event kernel are zero; and a maximum distance beyond which receivers can contribute fully to the kernel (receiver taper values in Table 1). To address the uneven station distribution, we followed the strategy proposed by Ruan et al. (2019) and applied weights to the misfit measurements based on the density of recording stations. In this scheme, isolated stations away from the source contribute fully to the event kernel and densely clustered stations contribute less. To address the high sensitivity of waveforms to near-source and near-receiver structure, we use a cut-out to simply set the kernel values to zero within a spherical volume around the source and receiver. The cut-out radii for each inversion stage are compiled in Table 1. Smoothing of the gradients for inversion (after summation of event kernels) was performed as described above with a diffusion equation applying an anisotropic smoothing operator with characteristic length scales proportional to the local v_{SV} wavelength. Finally, we applied the "Region of Interest" (ROI) approach described in Rodgers et al. (2022) to only solve for wavespeed updates below a certain depth for each inversion stage. This started at 25 km and was reduced and then eliminated as the inversion stages progressed. The relative misfit reductions within each stage of the six inversion stages are plotted in Figure 6. Within each inversion stage except the final (sixth) one we obtained 10-25% misfit reduction. Initial iterations in an inversion stage obtained larger reductions and these reductions decreased as the iterations approached convergence.

To measure performance in terms of waveform fits we computed the misfit reduction between the final (MESWA) and other models relative to the SPiRaL starting model in the final period band 30-100 seconds. For this analysis we computed both the time-frequency phase (TF) misfit used in the inversion and the normalized L2 (NL2) misfit for the windows selected with our final model. Figure 7a shows the average relative misfit reduction for all inversion events (sorted from high to low reduction corresponding to most to least improved fit). These show that some events have TF misfit reduction as high as 75% while others have only a smaller 10-20% misfit reduction. The average TF misfit is 59.7% and the NL2 misfits closely tracks the TF misfits with an average misfit of 55.3%. This is encouraging and quantifies the model performance in terms of the waveform misfit reduction for all data from the 192 events considered in the inversion. Also shown in Figure 7a are the event-averaged misfit reductions relative to the SPiRaL starting model of the two other models considered (MEC-1 and CSEM2.0).

These models perform much more poorly compared to SPiRaL and MESWA and these plots provide clear evidence that the choice of SPiRaL for the starting model was justified.

A more objective measure of model performance can be found by analyzing performance of MESWA with the independent validation data that was not used in the inversion. These paths (Figure 5b) are representative of the paths for the inversion data set shown in Figure 5a. The event-averaged relative misfit reductions for our MESWA model relative to the starting model for these events are shown in Figure 7b. The range of these misfit reductions are comparable with those of the inversion data set and the mean values are only slightly smaller (1-2%). This indicates that our final model provides waveform fits for the validation data set that are as good as those obtained in the inversion. This gives us confidence that the resulting model is not a result of overfitting the inversion data.

Another metric of model performance is seen in the time-bandwidth products (TBP) of selected waveform segments plotted in Figure 4. Our MESWA model consistently shows larger TBP than the SPiRaL (starting), MEC-1 or CSEM models, with the TBP values for MESWA about 40% higher than those for SPiRaL. This indicates that MESWA model produces simulated waveforms that agree better than the other models as measured by the selected window metrics. Note that the inversions described above were performed with a minimum period of 30 seconds in the sixth and final inversion stage. However, the TBP values show that the MESWA model has larger TBP values than the SPiRaL starting model across the bandwidth shown including periods shorter than 30 seconds. This suggests that the AWT approach adopted here provides models that can produce good waveform fits for shorter periods than those used in the inversions. It is appealing feature that AWT models provide good fits for periods shorter than those consider in the inversions.

Results

We now describe the results of the waveform inversions described in the previous section. We start by showing waveforms to illustrate the improved fits obtained with the inversions. This will be followed by presentation of the imaged shear wavespeed and anisotropy structure.

Waveform Fits

Firstly, we show waveforms for a few stations that recorded a single event and synthetics for the four models discussed: our MESWA (final inversion model); the SPiRaL (Simmons et al., 2021) starting model, MEC-1 (Kaviani et al., 2020) and CSEM (Noe et al., 2023). Figure 8a shows a map of an M_W 5.90 earthquake that occurred 2003-08-21 in Southern Iran along with selected stations that recorded the event with good signal-to-noise ratios on three components. The observed and synthetic waveforms for the four models are shown as record sections in Figure 8b-e. Waveforms shown in this section are scaled with distance but each pair of observed and synthetic are shown with true relative amplitudes. The MESWA model (Figure 8b) shows the best fits across distances and components compared to the other models: SPiRaL (Figure 8c); MEC-1 (Figure 8d) and CSEM (Figure 8e). Generally, waveform misfits (errors in phase alignment) tend to be small at short distances and increase with distance as phase errors causing misalignment to accumulate along the path or the entire 'banana-doughnut' sensitivity kernel of the waveform. The MEC-1 and CSEM models show clear phase errors approaching half a cycle or more for surface waves at the longest distances. Not surprisingly the MEC-1 model fits Love waves on the transverse component very poorly. Recall MEC-1 is based on Rayleigh wave and P-wave receiver function data, is most sensitive to vertically polarized shear wavespeeds, v_{SV}, and does not contain constraints on v_{SH}. MEC-1 also performs poorly for the body waves. The SPiRaL starting model fits the observed waveforms shown in Figure 8c better than the MEC-1 or CSEM models, consistent with the misfit reduction analyses presented in the previous section. However, the MESWA model fits the body waves and dispersed surface waves at long range better than SPiRaL, also consistent with the misfit reduction analyses. Note the good fit of first motions and amplitudes suggests the GCMT source parameters (i.e., moment tensor, depth, M_W) are reasonably good.

We show additional examples of waveform fits for the MESWA and SPiRaL models for a few events scattered around the domain with paths sampling the diverse tectonic structures of the region. Figure 9 shows an M_W 6.14 event in Crete, Greece (2011-04-01). The waveforms for the MESWA model (Figure 9b) show good fit to the Rayleigh waves at stations GO.AKH (Georgia), II.RAYN (Saudi Arabia) and II.ABKT (Turkmenistan). In particular the path to II.ABKT is better fit by MESWA (Figure 9b) than SPiRaL (Figure 9c) for a path crossing the thick sediments of the Caspian Sea known to complicate surface wave propagation (Priestley et al, 2001).

Figure 10 shows an M_W 5.98 event on the Turkey-Iran border region (2020-02-23). The fundamental mode surface waves are well-fit by the MESWA model, particularly at longer distances. Phases errors for Rayleigh waves for the SPiRaL model (Figure 10c) at stations CQ.PARA (Cyprus), KO.GULT (Türkiye), HT.ALN and HL.VAM (Greece) are corrected for MESWA (Figure 10b). Paths crossing the Caspian Sea to Central Asia (KR.BTK, KR.ARSB. KR.NRN, Kyrgyzstan) show better agreement of the fundamental mode and scattered surface waves for the MESWA model (Figure 10b). Similar results are seen for an M_W 6.04 Afghanistan-Tajikistan border region (2001-11-23) shown in Figure 11. The paths crossing the Caspian Sea: IU.GNI (Armenia); II.KIV (Georgia); GE.ISP (Türkiye) are well fit by the MESWA model as are paths crossing the Iranian Plateau and Zagros Mountains: GE.CSS (Cyprus) and II.RAYN (Saudi Arabia).

Finally, we show two events from the southwestern and southern parts of the domain: an M_W 5.54 Red Sea (2013-07-08) in Figure 12 and an M_W 5.96 Eastern Gulf of Aden (2002-09-01) in Figure 13. These events provide paths crossing the Arabian Shield and Arabian Platform at closest distances with some paths extending across the Turkish and Iranian Plateaus and beyond. The closest paths sampling Arabia and more distant paths sampling adjacent tectonic regions are better fit by the MESWA model than SPiRaL. The paths from the Red Sea to central Asia (IU.KBL, Kabul Afghanistan; 5C.MAR2, Tajikistan; and KR.BTK, Kyrgyzstan) show Rayleigh waves poorly fit by SPiRaL (Figure 12b) that are fit better by MESWA (Figure 12c). The path from the Gulf of Aden to II.ABKT (Turkmenistan) crossing the Arabian Platform, continental collision along the Zagros Mountains and Central Iran Block is poorly fit by SPiRaL with phase errors for the Rayleigh waves approaching half a cycle (Figure 13c). However, the accumulated phase errors for this long path are adjusted by the iterative waveform inversion performed here and the resulting MESWA model fits the waveforms better (Figure 13b). Nonetheless there are dispersed, later arriving and shorter period surface waves that could be fit better with additional inversion iterations and more data.

Maps and Cross-Sections

We now show the imaged 3D structure as the isotropic shear wavespeed, $v_S = \sqrt{\frac{v_{SH}^2+2v_{SV}^2}{3}}$, and anisotropy parameter, $\xi_S = \left(\frac{v_{SH}}{v_{SV}}\right)^2$, (Panning and Romanowicz, 2006). Figure 14-18 show the v_S and ξ_S structure in mapview for the SPiRaL and MESWA models and the natural logarithm ratio (MESWA/SPiRaL) at depths of 2, 10, 30, 60 and 100 km below to sea level. As shown below the MESWA model is broadly similar to the SPiRal starting model, but adjustments made to the 3D wavespeed structure during the multiscale waveform inversion process have improved the waveform fits as described in the previous sections. Generally the updates to the SPiRaL model obtained with the adjoint waveform tomography methodology described above tends to increase the amplitude of lateral variations in v_S and ξ_S structure and reduce the scale-length of variations.

At 2 km in the upper crust (Figure 14) the main adjustments to SPiRaL (Figure 14c) are a reduction by more than 5% of v_S in the sedimentary structures of the eastern Mediterranean Sea, Caspian Sea, Arabian Platform, the (Arabian/Persian) Gulf and the continental margins. Shear wavespeeds for MESWA are increased relative to SPiRaL at this depth for the Turkish Plateau, Central Iran Block and Central Afghan Highlands. MESWA also reveals a general reduction of ξ_S across the domain (Figure 14f). At this depth $\xi_S < 1$ ($v_{SV} > v_{SH}$) for most of the continental regions. Note that at this depth adjustments are only made to the solid Earth with topography and bathymetry above 2 km below sea level.

Figure 15 shows the v_S and ξ_S structure at 10 km below sea level. At this depth shear wavespeeds are broadly similar between SPiRaL (Figure 15a) and MESWA (Figure 15b). The oceanic regions (Arabian Sea, Gulf of Aden, Red Sea) have much higher v_S values corresponding to lower crust or mantle material, while the continental regions show lower v_S values with significant variability (standard deviation of about 7%). Adjustments to v_S structure also show reductions of 5% or more in regions of sedimentary basins (eastern Mediterranean Sea, Caspian Sea and Arabian Platform, Gulf) similar to 2 km depths and suggesting the long-period waveforms considered here are weakly sensitive to shallow crustal structure. At this depth the waveform inversion process requires the scale-length of wavespeed adjustments to v_S and ξ_S (Figure 15c and 15e) to have shorter wavelength variability that for SPiRaL. The MESWA model shows a band of low v_S values tracing a long arc across the Turkish Plateau, Zagros and Alborz Mountains and the Sulaiman Fold Belt.

The 30 km depth cuts through the continental Moho and the oceanic regions are clearly represented by mantle v_S values (> 4000 m/s, Figure 16). Low v_S values are seen in the Turkish-Iranian Plateau, Afghanistan, Pakistan and the Hindu Kush corresponding to thickened continental crust. The Arabian Shield reveals higher v_S values than the Arabian Platform as seen in previous waveform modeling studies (Rodgers et al., 1999).

At 60 km depth the MESWA model reveals low v_S values surround much of the Arabian Plate along the active spreading centers of the Red Sea, Gulf of Aden and Owen Fracture Zone, the Ethiopian/Afar Hotspot as well as the continental transform of the Dead Sea Fault (Figure 17b). These areas of low v_S were intensified from the SPiRaL model as seen in the natural logarithm ratio map (Figure 17c). Low v_S values underlaying the Arabian Shield and Afar as has been reported in several tomographic studies (e.g. Park et al., 2007; 2008; Hansen and Nyblade, 2013). These low v_S values at mantle depths follow the Mecca-Madina-Nafud (MMN) volcanic line. Higher v_S values were intensified at this depth in the Zagros Mountains, Central Iran Block and Makran subduction zone (Figure 16c).

The low v_S values seen at 60 km are broadly similar to those seen at 100 km depth (Figure 18b). The high v_S underlaying the eastern Arabian Platform and Zagros Mountains at 60 and 100 km depth is consistent with strong continental lithosphere participating in active continental collision. Higher than average v_S follows Makran subduction at mantle depths (Figures 17b and 18b).

We now visualize the SPiRaL and MESWA models with cross-sections of the isotropic shear wavespeed, v_S, and anisotropy parameter ξ_S. Figure 19 shows cross-sections and locations: A-A’ a west-east section along latitude of 34°; and B-B’ is a west-east section along longitude of 28°. For each section we show the v_S and ξ_S structure of the SPiRaL starting model and our final MESWA model from the surface to a depth of 400 km. The A-A’ section cuts through the Hellenic Back-Arc, Turkish Plateau, Iranian Plateau, Caspian Sea, Kopet Dagh, Turan Platform and Hindu Kush (Figure 19a). Transitions in the v_S structure clearly mark the geologic/tectonic boundaries. As seen above in the map view plots (Figures 14-18), the MESWA model intensifies the high and low v_S anomalies, sharpens some boundaries and adds smaller scale variations, particularly in ξ_S, relative to SPiRaL. Positive anisotropy ($v_{SH} > v_{SV}$) is revealed under southern Caspian Sea, Kopet Dagh and Turan Platform.

The B-B' cross-section (Figure 19d) crosses the Nubian Shield, northern Red Sea, Arabian Shield, Arabian Platform, Zagros Mountains, Makran subduction zone, Sulaiman Fold Belt to the Indian Shield. The Red Sea and Arabian Shield are underlain by low v_S, consistent with thin lithosphere (e.g. Hansen et al., 2008). The Arabian Platform and Zagros Mountains are underlain by high v_S, with the strongest feature just north of the Straights of Hormuz separating the Zagros continental collision from the Makran oceanic subduction. High v_S is continuous under the Makran and Indus River Plain on the Indian Shield. The positive radial anisotropy is strongest under the eastern Arabian Platform, Gulf and Zagros Mountains.

We show south-north sections in Figure 20. The C-C' south-north section along longitude of 44° cuts through the Afar Hotspot, the Arabian Shield, the Arabian Platform, Turkish-Iranian Plateau, Caucasus and stable Eurasian Plate (Figure 20a). Broadly, MESWA v_S anomalies track SPiRaL with some adjustments, but the ξ_S structure of MESWA shows smaller scale features relative to SPiRaL (Figure 20bc). The boundary between the Arabian Shield and Platform is sharper and more vertical in the MESWA image on this longitude. The shallow mantle under the Turkish-Iranian Plateau reveals low v_S and closely follows the Bitlis Suture marking the Arabian-Eurasian plate boundary. Low v_S in this region is associated with low Pn wavespeeds and high Sn attenuation (e.g. Hearn and Ni, 1993; Rodgers et al., 1997). This low mantle v_S feature continues north to the boundary between the Caucasus Mountains and the Scythian Platform (Russia).

The south-north cross-section along longitude 60° crosses the Owen Fracture Zone, perpendicular to the strike of Makran subduction, the Lut Block, eastern Iran, the Kopet Dagh and Turan Platform. The Owen Fracture Zone is underlain by low v_S in the upper 200 km of the mantle and this continues north to the Makran subduction zone. High v_S is imaged beneath the Makran as a continuous feature from below the Moho to 400 km depth. Eastern Iran is underlain by low v_S, at depths of 100-300 km in the upper mantle extending north of the Kopet Dagh into the Turan Platform. Strong positive anisotropy us imaged beneath the Turan Platform (Figure 20f).

Conclusions

In this study we applied adjoint tomography to a large region of the Middle East and southwest Asia using only openly available broadband waveform data. The multiscale inversion approach results in modifications to the SPiRaL starting (Simmons et al., 2021) and the minimum period of waveforms is reduced from 50 seconds to 30 seconds. While it may be possible to further reduce the minimum period the highly uneven path coverage of the limited openly available data may not support resolution of smaller-scale features. The resulting model provide quantitatively better waveform fits in terms of the time-bandwidth product (information content, Figure 4) and misfit measurements (Figure 7). This is illustrated in example waveform fits for paths sampling the diverse tectonic provinces of study area (Figures 8-12). The imaged structure is illustrated in the isotropic shear wavespeed, v_S, and anisotropy parameter, x_S, as shown in map view (Figures 14-18) and cross-sections (Figures 19-20). We see strong correlation of the imaged v_S structure with tectonic/geologic features as is seen in the SPiRaL model. Relative to the SPiRaL starting model, MESWA generally infers smaller scale-length variation of shear wavespeeds and much smaller scale-length variations in anisotropy. We also see the amplitude of shear wavespeed anomalies tends to increase (i.e., higher highs and lower lows).

The MESWA model presented in this report shows what can be done with earthquake waveform tomography in a region with highly uneven coverage of openly available broadband data. The event (Figure 1) and station (Figures 2) coverage are dense in some regions and non-existent in others. Figure 5a shows the path coverage used in the inversion. This case is well-suited for the station weighting scheme used in previous inversions (e.g. Wehner et al. 2020; Rodgers et al., 2022; Doody et al. 2023). In this scheme, misfits from areas of dense station sampling are down-weighted and areas of sparse sampling are upweighted. These weights directly impact the contributions to the gradients so that we do not fit data in densely sampled region at the expense of sparsely sampled regions.

The MESWA model presented in this report demonstrates effective improvements in waveform fits for minimum periods of 30 seconds. The time-bandwidth product (TBP) measured from picked windows shows that MESWA produces longer time-segments of good waveform correlations for periods below 30 seconds compared to the other models considered (Figure 4). It remains for further work to continue inversion iterations with the current openly available data set to investigate if further details can be imaged. Alternatively, adding waveform data from the many seismic networks from the region that do not make their data available (so-called "closed" networks) could greatly improve the resolution of smaller scale-length features, reduce the minimum period and increase the TBP of waveform fits. Many tomography and structural studies of the region have shown the values of closed network data for imaging details of seismic wavespeed variations. We expect similar benefits would be found applying adjoint waveform tomography with closed network data folded into the analysis of open data described here.

Finally, the MESWA model described in this study could be used for long-period waveform simulations. The most important practical application of the model could be for source characterization using moment tensor inversion. Greens functions for 3D models have been shown to provide better waveform fits and reduced uncertainties in source type estimate inversion (Liu et al., 2004; Covellone and Savage, 2012; Zhu and Zhou, 2016; Sawade et al., 2022; Chiang et al., 2023; Doody et al., 2023). For example, the MESWA model could be used to model the 1998 nuclear explosions in India and Pakistan (Barker et al., 1998) or sub-crustal events in the Zagros Mountains and Makran subduction zone (e.g. Engdahl et al., 2006).

Acknowledgements

This work was initiated under Laboratory Directed Research and Development project 20-ERD-008 at Lawrence Livermore National Laboratory and completed with support from the National Nuclear Security Administration. Simulations were performed on the Lassen graphics-processing unit accelerated platform operated by Livermore Computing at LLNL with access for this work coming from the Institutional Computing Grand Challenge program. This work was performed under the auspices of the U.S. Department of Energy by Lawrence Livermore National Laboratory under Contract DE-AC52-07NA27344. This is LLNL contribution LLNL-TR-851939-DRAFT.

Data Availability Statement

All earthquake and network/seismic data used in this study are listed in the data repository Rodgers (2023). Waveform forward and inverse simulations were performed with Salvus (mondaic.com). Nathan Simmons provided the SPiRaL model (Simmons et al., 2021). The Midd_East_Crust_1 (Kaviani et al., 2020) model was obtained from the Incorporated Research Institutions for Seismology Earth Model Collaboratory (http://ds.iris.edu/ds/products/emc-earthmodels). The CSEM2 model was provided by Sebastian Noe (Eidgenössische Technische Hochschule, Zurich, Switzerland). The MESWA model described in this report will be made available in the data repository.

References

Afanasiev, M., D. Peter, K. Sager, S. Simutė, L. Ermert, L. Krischer and A. Fichtner (2016). Foundations for a multiscale collaborative Earth model, *Geophys. J. Int.*, 204(1), 39–58, https://doi.org/10.1093/gji/ggv439

Afanasiev, M, C Boehm, M van Driel, L Krischer, M Rietmann, D. A. May, M. G. Knepley and A. Fichtner (2019). Modular and flexible spectral-element waveform modelling in two and three dimensions, *Geophys. J. Int.*, 216(3), 1675–1692, doi: 10.1093/gji/ggy469

Al-Damegh, K., E. Sandvol and M. Barazangi (2005). Crustal structure of the Arabian plate: new constraints from the analysis of teleseismic receiver functions, *Earth Planet. Sci. Lett.*, 231, (3-4), 177-196, https://doi.org/10.1016/j.epsl.2004.12.020.

Al-Lazki, A. I., Seber, D., Sandvol, E., Turkelli, N., Mohamad, R., and Barazangi, M. (2003). Tomographic Pn velocity and anisotropy structure beneath the Anatolian plateau (eastern Turkey) and the surrounding regions, *Geophys. Res. Lett.*, 30, 8043, doi:10.1029/2003GL017391,

Al-Lazki, A.I., Sandvol, E., Seber, D., Barazangi, M., Turkelli, N. and Mohamad, R. (2004), *Pn* tomographic imaging of mantle lid velocity and anisotropy at the junction of the Arabian, Eurasian and African plates. Geophysical Journal International, 158: 1024-1040. https://doi.org/10.1111/j.1365-246X.2004.02355.x

Al-Lazki, A.I., K. S. Al-Damegh , S. Y. El-Hadidy, A. Ghods , and M. Tatar (2014). *Pn*-velocity structure beneath Arabia–Eurasia Zagros collision and Makran subduction zones, *Geological Society, London, Special Publications* (2014), 392 (1): 45, https://doi.org/10.1144/SP392.3

Brian Barker et al. (1998). Monitoring Nuclear Tests. *Science*, 281, 1967-1968, DOI:10.1126/science.281.5385.1967

Blom, N., C. Boehm & A. Fichtner (2017). Synthetic inversions for density using seismic and gravity data, *Geophys. J. Int.*, 209(2), 1204–1220, https://doi.org/10.1093/gji/ggx076

Bozdağ, E., J. Trampert & J. Tromp (2011). Misfit functions for full waveform inversion based on instantaneous phase and envelope measurements, *Geophys. J. Int.*, 185(2), 845–870, https://doi.org/10.1111/j.1365-246X.2011.04970.x

Bozdağ, E., D. Peter, M. Lefebvre, D. Komatitsch, J. Tromp, J. Hill, N. Podhorszki, D. Pugmire (2016). Global adjoint tomography: first-generation model, *Geophys. J. Int.*, 207(3), 1739–1766, https://doi.org/10.1093/gji/ggw356

Boehm, C., N. K. Martiartu, N. Vinard, I. Jovanović Balic & A. Fichtner (2018). Time-domain spectral-element ultrasound waveform tomography using a stochastic quasi-Newton method, Medical Imaging 2018: Ultrasonic Imaging and Tomography, N. Duric and B. C. Byram eds., International Society for Optics and Photonics, SPIE, 10580, 92-100, doi:10.1117/12.2293299

Brocher, T.M. (2005). Empirical relations between elastic wavespeeds and density in the earth's crust. *Bulletin of the Seismological Society of America*, 95 (6): 2081–2092. doi: https://doi.org/10.1785/0120050077

Bunks, C., Saleck, F.M., Zaleski, S. and Chavent, G. (1995). Multiscale Seismic Waveform Inversion. *Geophysics*, 60, 1457-1473. https://doi.org/10.1190/1.1443880

Chiang, A., A. Rodgers, L. Krischer, M. Afanasiev, C. Boehm, N. Simmons and C. Doody (2023). Regional moment tensor inversion of the Western United States using a three-dimensional Earth model, (manuscript in preparation).

Chang, S.-J., van der Lee, S., Flanagan, M. P., Bedle, H., Marone, F., Matzel, E. M., Pasyanos, M. E., Rodgers, A. J., Romanowicz, B., and Schmid, C. (2010a), Joint inversion for three-dimensional *S* velocity mantle structure along the Tethyan margin, *J. Geophys. Res.*, 115, B08309, doi:10.1029/2009JB007204.

Chang, S.-J., Van Der Lee, S., Matzel, E. and Bedle, H. (2010b), Radial anisotropy along the Tethyan margin. Geophys. J. Int., 182, 1013-1024, https://doi.org/10.1111/j.1365-246X.2010.04662.x

Conn, A.R., N.I.M. Gould & P. L. Toint (2000). Trust Region Methods, SIAM-MPS, Philadelphia, USA

Covellone, B.M. and B. Savage (2012). A Quantitative Comparison between 1D and 3D Source Inversion Methodologies: Application to the Middle East. *Bull. Seismol. Soc. Am.*, 102 (5): 2189–2199. doi: https://doi.org/10.1785/0120110278

Doody, C., Rodgers, A., Afanasiev, M., Boehm, C., Krischer, L., Chiang, A., & Simmons, N. (2023). Comparing adjoint waveform tomography models of California using different starting models. *Journal of Geophysical Research: Solid Earth*, 128, e2023JB026463. https://doi.org/10.1029/2023JB026463

Doody, C., A. Chiang, A. Rodgers et al. (2023) Moment Tensor Catalogue for California and Nevada Using 3D Green’s Functions, (manuscript in preparation)

Dziewonski, A.M. and D. L. Anderson (1981). Preliminary Reference Earth Model, *Phys. Earth Planet. Int.*, 25, 297– 356, 1981.

Ekström, G., M. Nettles, & A. M. Dziewonski (2012). The global CMT project 2004-2010: Centroid-moment tensors for 13,017 earthquakes, *Phys. Earth Planet. Inter*., 200-201, 1-9. doi:10.1016/j.pepi.2012.04.002

Engdahl, E.R., J.A. Jackson, S.C. Myers, E.A. Bergman and K. Priestley (2006). Relocation and assessment of seismicity in the Iran region, *Geophys. J. Int.*, 167(2), 761–778, https://doi.org/10.1111/j.1365-246X.2006.03127.x

Fichtner, A. (2010). Full seismic waveform modelling and inversion. Berlin, Heidelberg: Springer.

Fichtner, A., Bunge, H.-P., & Igel, H. (2006). The adjoint method in seismology I. Theory, Phys. Earth Planet. Int., 157(1–2), 86–104.

Fichtner, A., B. L. N. Kennett, H. Igel & H.-P. Bunge (2008). Theoretical background for continental- and global-scale full-waveform inversion in the time–frequency domain, *Geophys. J. Int.*, 175(2), https://doi.org/10.1111/j.1365-246X.2008.03923.x

Fichtner, A., Kennett, B.L.N., Igel, H., Bunge, H.P. (2009). Full seismic waveform tomog- raphy for upper-mantle structure in the Australasian region using adjoint methods. *Geophysical Journal International*, 179, 1703–1725.

Fichtner, A., Trampert, J., Cupillard, P., Saygin, E., Taymaz, T., Capdeville, Y., & Villasenor, A. (2013). Multiscale full waveform inversion. *Geophys. J. Int*., 194, 534–556.

Fichtner, A., van Herwaarden, D.-P., Afanasiev, M., Simutė, S., Krischer, L., Çubuk-Sabuncu, Y., et al. (2018). The Collaborative Seismic Earth Model: Generation 1. *Geophysical Research Letters*, 45, 4007– 4016. https://doi.org/10.1029/2018GL077338

Gaherty, J.B. and Jordan, T.H., 1995. Lehmann discontinuity as the base of an anisotropic layer beneath continents. *Science*, *268*(5216), pp.1468-1471.

Gee, L. S., & T. H. Jordan (1992), Generalized seismological data functionals, Geophys. J. Int.,111(2), 363–390, https://doi.org/10.1111/j.1365-246X.1992.tb00584.x

Hansen, S., S. Schwartz, A. Al-Amri and A. Rodgers (2006). Combined plate motion and density-driven flow in the asthenosphere beneath Saudi Arabia: Evidence from shear-wave splitting and seismic anisotropy. *Geology*, 34 (10): 869–872. doi: https://doi.org/10.1130/G22713.1

Hansen, S.E., A.J. Rodgers, S.Y. Schwartz, A.M.S. Al-Amri (2007). Imaging ruptured lithosphere beneath the Red Sea and Arabian Peninsula, *Earth and Planetary Science Letters*, 259, 256-265, https://doi.org/10.1016/j.epsl.2007.04.035.

Hansen, S.E. and A. A. Nyblade (2013). The deep seismic structure of the Ethiopia/Afar hotspot and the African superplume, *Geophys. J. Int.*, 194(1), 118–124, https://doi.org/10.1093/gji/ggt116

Hearn, T. M., & Ni, J. F. (1994). Pn velocities beneath continental collision zones: the Turkish-Iranian Plateau. *Geophysical Journal International*, *117*(2), 273-283.

Julià, J., C. J. Ammon, R. B. Herrmann (2003). Lithospheric structure of the Arabian Shield from the joint inversion of receiver functions and surface-wave group velocities, *Tectonophysics*, 371, 1-21, https://doi.org/10.1016/S0040-1951(03)00196-3.

Kaviani, A., Paul, A., Moradi, A., Mai, P. M., Pilia, S., Boschi, L., Rümpker, G., Lu, Y., Tang, Z., and Sandvol, E., 2020, Crustal and uppermost mantle shear-wave velocity structure beneath the Middle East from surface-wave tomography: Geophys. J. Int., https://doi.org/10.1093/gji/ggaa075.

Kim, R., M. Witek, S.-J. Chang, J.-A Lim, P. Martin Mai, H. Zahran (2023). Isotropic and radially anisotropic S-velocity structure beneath the Arabian plate inferred from surface wave tomography, *Tectonophysics*, 862, 229968, https://doi.org/10.1016/j.tecto.2023.229968.

Komatitsch, D. & J. Tromp (2002a). Spectral-element simulations of global seismic wave propagation—I. Validation, *Geophys. J. Int.*, 149(2), 390–412, https://doi.org/10.1046/j.1365-246X.2002.01653.x

Komatitsch, D. & J. Tromp (2002b). Spectral-element simulations of global seismic wave propagation—II. Three-dimensional models, oceans, rotation and self-gravitation, *Geophys. J. Int.*, 150(1), 303–318, https://doi.org/10.1046/j.1365-246X.2002.01716.x

Krischer, L., T. Megies, R. Barsch, M. Beyreuther, T. Lecocq, C. Caudron & J. Wassermann (2015a). ObsPy: a bridge for seismology into the scientific Python ecosystem, *Comput. Sci. Discovery*, 8(1), 14,003-14,020, doi:10.1088/1749-4699/8/1/014003

Krischer, L., A. Fichtner, S. Zukauskaite & H. Igel (2015b). Large-Scale Seismic Inversion Framework. *Seismo. Res. Lett.,* 86 (4) 1198–1207. doi: 10.1785/0220140248

Krischer, L., J. Smith, W. Lei, M. Lefebvre, Y. Ruan, E. Sales de Andrade, N. Podhorszki, E. Bozdağ, & J. Tromp (2016) An Adaptable Seismic Data Format, *Geophys. J. Int.,* 207(2), 1003–1011, doi: 10.1093/gji/ggw319

Kristeková, M., J. Kristek, P. Moczo & S.M. Day (2006). Misfit Criteria for Quantitative Comparison of Seismograms. *Bull. Seismo. Soc. Am.*, 96 (5), 1836–1850.https://doi.org/10.1785/0120060012

Kristeková, M., J. Kristek & P. Moczo (2009). Time-frequency misfit and goodness-of-fit criteria for quantitative comparison of time signals, *Geophys. J. Int.,* 178(2), 813–825, https://doi.org/10.1111/j.1365-246X.2009.04177.x

Laske, G., G. Masters, Z. Ma and M. Pasyanos (2013). Update on CRUST1.0 – A 1-degree Global Model of Earth's Crust, Geophys. Res. Abstracts, 15, Abstract EGU2013-2658,.

Liu, Q., J. Polet, D. Komatitsch and J. Tromp (2004). Spectral-Element Moment Tensor Inversions for Earthquakes in Southern California. *Bull. Seismol. Soc. Am.*, 94 (5): 1748–1761. doi: https://doi.org/10.1785/012004038

Liu, Q., & Tromp, J. (2008). Finite-frequency sensitivity kernels for global seismic wave propagation based upon adjoint methods. Geophys. J. Int., 174(1), 265–286. https://doi.org/10.1111/j.1365-246X.2008.03798.x

Liu, Q. and Y.J. Gu (2012). Seismic imaging: From classical to adjoint tomography, *Tectonophysics*, 566–567, 31-66, https://doi.org/10.1016/j.tecto.2012.07.006.

Maggi, A. and K. Priestley (2005). Surface waveform tomography of the Turkish–Iranian plateau, *Geophys. J. Int.*, 160 (3), 1068–1080, https://doi.org/10.1111/j.1365-246X.2005.02505.x

Maggi, A., C. Tape, M. Chen, D. Chao, & J. Tromp. An automated time-window selection algorithm for seismic tomography. Geophys. J. Int., 178:257–281, 2009

Modrak, R. & J. Tromp (2016). Seismic waveform inversion best practices: regional, global and exploration test cases, *Geophys. J. Int.*, 206(3), 1864–1889, doi:10.1093/gji/ggw202

Modrak, R.T., D. Borisov, M. Lefebvre, & J. Tromp (2018). SeisFlows—Flexible waveform inversion software, *Computers & Geosciences*, 115, 88-95, doi: 10.1016/j.cageo.2018.02.004.

Mokhtar, T. A., Ammon, C. J., Herrmann, R. B., & Ghalib, H. A. A. (2001). Surface wave velocities across Arabia. In *Monitoring the Comprehensive Nuclear-Test-Ban Treaty: Surface Waves* (pp. 1425-1444). Birkhäuser, Basel.

Movaghari, R. and G. Javan Doloei (2020). 3-D crustal structure of the Iran plateau using phase velocity ambient noise tomography, *Geophs. J. Int.*, 220(3), 1555–1568, https://doi.org/10.1093/gji/ggz537

Nocedal, J. & S. Wright (2006). Numerical Optimization, Springer, New York, USA

Noe, S., D. Van Herwaarden, S. Thrastarson, Y. Gao, F. Tilmann, J. Ma, H. Bunge, H., N. Masouminia, D. Wehner, A. Rodgers and A. Fichtner (2022). The Collaborative Seismic Earth Model: Generation 2 (abstract), Seismic Tomography: What Comes Next?

Panning, M & B. Romanowicz (2006). A three-dimensional radially anisotropic model of shear velocity in the whole mantle, *Geophys. J. Int.*, 167(1), 361–379, https://doi.org/10.1111/j.1365-246X.2006.03100.x

Park, Y., Nyblade, A. A., Rodgers, A. J., and Al-Amri, A. (2007), Upper mantle structure beneath the Arabian Peninsula and northern Red Sea from teleseismic body wave tomography:

Implications for the origin of Cenozoic uplift and volcanism in the Arabian Shield, *Geochem. Geophys. Geosyst.*, 8, Q06021, doi:10.1029/2006GC001566.

Park, Y., Nyblade, A. A., Rodgers, A. J., and Al-Amri, A. (2008), S wave velocity structure of the Arabian Shield upper mantle from Rayleigh wave tomography, *Geochem. Geophys. Geosyst.*, 9, Q07020, doi:10.1029/2007GC001895.

Płonka, A., Blom, N., & Fichtner, A. (2016). The imprint of crustal density heterogeneities on regional seismic wave propagation. Solid Earth, 7(6), 1591–1608. https://doi.org/10.5194/se-7-1591-2016

Priestley, K., H. J. Patton, C. A. Schultz (2001). Modeling Anomalous Surface-Wave Propagation across the Southern Caspian Basin. *Bull. Seismol. Soc. Amer.,* 91(6), 1924–1929, https://doi.org/10.1785/0120010118

Rodgers, A., W. Walter, R. Mellors, A.M.S. Al-Amri, Y.-S. Zhang, Yu-Shen (1999). Lithospheric structure of the Arabian Shield and Platform from complete regional waveform modelling and surface wave group velocities, *Geophys. J. Int.*, 138(3), 871–878, https://doi.org/10.1046/j.1365-246x.1999.00918.x

Rodgers, A., L. Krischer, M. Afanasiev, C. Boehm, C. Doody, A. Chiang, N. Simmons (2022). WUS256: An Adjoint Waveform Tomography Model of the Crust and Upper Mantle of the Western United States for Improved Waveform Simulations, J. Geophys. Res., https://doi.org/10.1029/2022JB024549

Rodgers, A.J. (2023). Dataset for "MESWA: Seismic structure of the crust and upper mantle of the middle east and southwest asia from adjoint waveform tomography using openly available broadband data". [Dataset]. Zenodo. https://doi.org????

Ruan, Y., Lei, W., Modrak, R., Örsvuran, R., Bozdağ, E., & Tromp, J. (2019). Balancing unevenly distributed data in seismic tomography: A global adjoint tomography example. Geophysical Journal International, 219(2), 1225–1236. https://doi.org/10.1093/gji/ggz356

Simmons N. A., S. C. Myers, C. Morency, A. Chiang, and D. R. Knapp (2021). SPiRaL: A multi-resolution global tomography model of seismic wave speeds and radial anisotropy variations in the crust and mantle, Geophys. J. Int., 227(2), 1366-1391, doi:/https://doi.org/10.1093/gji/ggab277

Sawade, L., S. Beller, W. Lei, Jeroen Tromp (2022). Global centroid moment tensor solutions in a heterogeneous earth: the CMT3D catalogue, *Geophysical Journal International*, 231 ,1727–1738, https://doi.org/10.1093/gji/ggac280

Tang, Z., Mai, P. M., Julià, J., & Zahran, H. (2019). Shear velocity structure beneath Saudi Arabia from the joint inversion of *P* and *S* wave receiver functions, and Rayleigh wave group velocity dispersion data. *Journal of Geophysical Research: Solid Earth*, 124, 4767– 4787. https://doi.org/10.1029/2018JB017131

Tarantola, A. (1988). Theoretical background for the inversion of seismic waveforms including elasticity and attenuation. *Pure and Applied Geophysics PAGEOPH*, 128, 365-399 doi:10.1007/bf01772605

Tape, C., Q. Liu, A. Maggi & J. Tromp (2010), Seismic tomography of the southern California crust based on spectral-element and adjoint methods, Geophys. J. Int.,180(1), 433–462, doi:10.1111/j.1365-246X.2009.04429.x

Tkalčić, H., Pasyanos, M. E., Rodgers, A. J., Gök, R., Walter, W. R., and Al-Amri, A. (2006), A multistep approach for joint modeling of surface wave dispersion and teleseismic receiver functions: Implications for lithospheric structure of the Arabian Peninsula, *J. Geophys. Res.*, 111, B11311, doi:10.1029/2005JB004130.

Tromp, J., C. Tape, & Q. Liu. (2005). Seismic tomography, adjoint methods, time reversal, and banana-donut kernels, *Geophys. J. Int.*, **160** 195–216. doi: 10.1111/j.1365-246X.2004.02453.x

Tromp, J. (2020). Seismic wavefield imaging of Earth's interior across the scales, *Nature Reviews,* **1**, 40-53 . doi: 10.1038/s43017-019-0003-8

Villasenor, A., Ritzwoller, M. H., Levshin, A. L., Barmin, M. P., Engdahl, E. R., Spakman, W., & Trampert, J. (2001). Shear velocity structure of central Eurasia from inversion of surface wave velocities. *Phys. Earth and Planet. Int.*, *123*(2-4), 169-184.

Wehner, D., N. Blom, N. Rawlinson, Daryono, C. Boehm, M. Miller, P. Supendi, & S. Widiyantoro (2022) 3-D Seismic Structural Model of the Lithosphere and Underlying Mantle Beneath Southeast Asia from Multi-Scale Adjoint Waveform Tomography. *Journal of Geophysical Research: Solid Earth, 127,* e2021JB022930. https://doi.org/10.1029/2021JB022930

Zhu, H., Bozdağ, E., & Tromp, J. (2015). Seismic structure of the European upper mantle based on adjoint tomography. *Geophys. J. Int.,* 201(1), 18–52. https://doi.org/10.1093/gji/ggu492

Figures and Captions

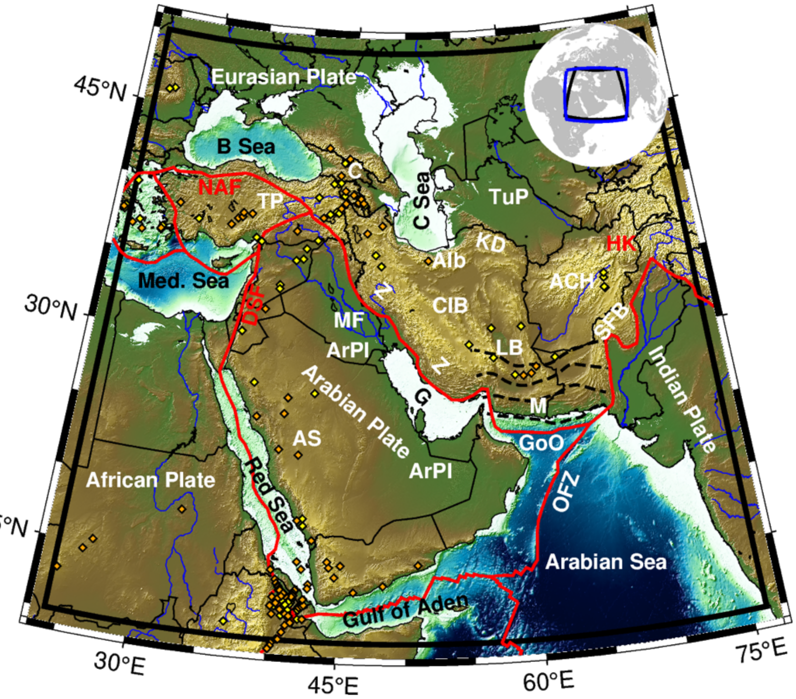

Figure 1. Map of the Middle East and Southwest Asia (MESWA) study area showing major geologic provinces (labels), tectonic plate boundaries (red lines), Pleistocene and Holocene volcanic centers (yellow and orange diamonds, respectively). Abbreviations for tectonic features are: ACP, Afghanistan Central Highlands; Alb, Alborz Mountains; ArPl, Arbaian Platform; AS, Arabian Shield; B Sea, Black Sea; C, Caucasus; CIB, Central Iranian Block; GoO, Gulf of Oman; HK, Hindu Kush; KD, Kopet Dag; LB, Lut Block; Med. Sea, Mediterranean Sea; MF, Mesopotamian Foredeep; NAF, North Anatolian Fault; OFZ, Owen Fracture Zone; SFB, Sulaiman Fold Belt; TP, Turkish Plateau; TuP, Turan Platform; Z, Zagros Mountains. The inset global map shows the Salvus domain (blue line) with the target domain (black line).

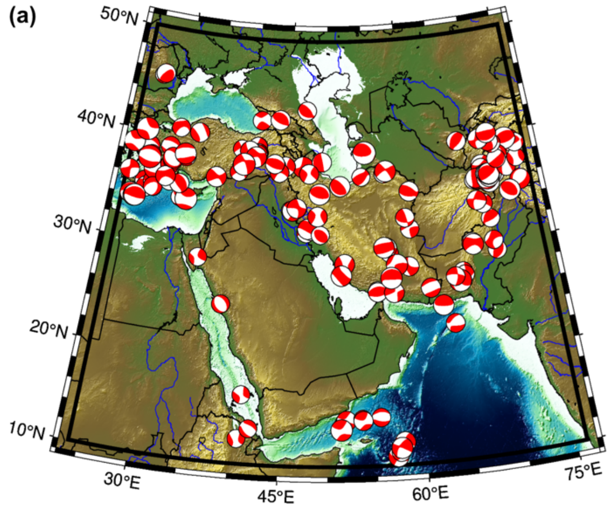

Figure 2. Maps of earthquake moment tensors for **(a)** 192 events used in the inversion and **(b)** 66 events used for validation.

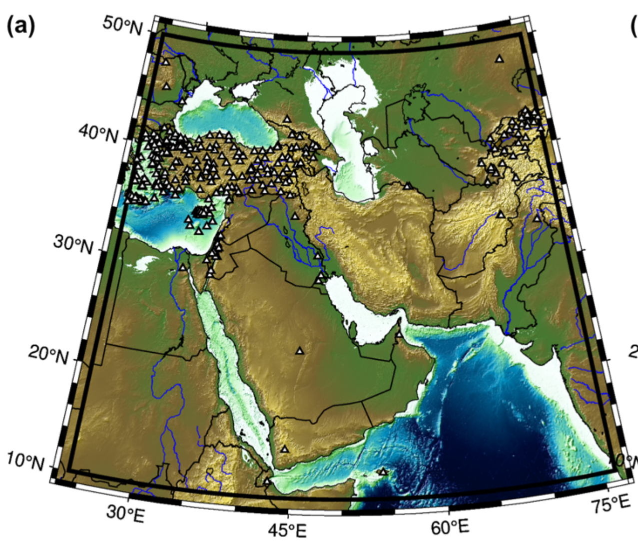

Figure 3. Map of the open access seismic stations used in this study for **(a)** permanent and **(b)** temporary networks.

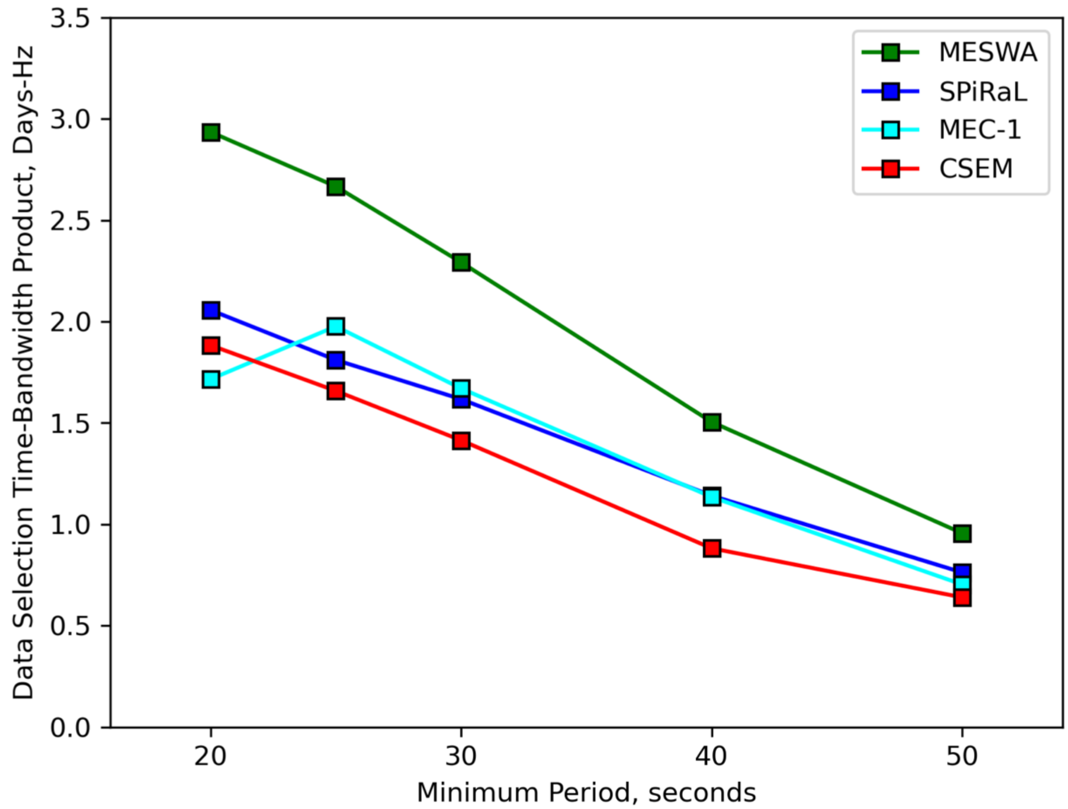

Figure 4. Time-bandwidth product versus minimum period for windows selected by comparing observed and simulated waveforms for over 320 events. The models are discussed in the text: SPiRaL (Simmons et al., 2021); MEC-1 (Kaviani et al. 2020); CSEM (Noe et al., 2023) and MESWA (this study).

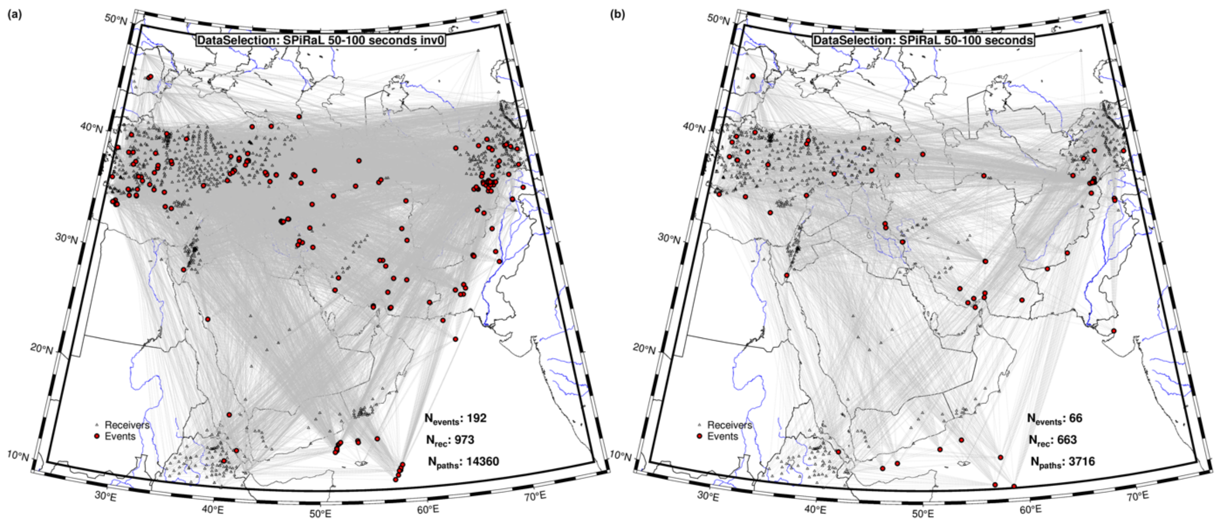

Figure 5. Map of events, stations and paths for the **(a)** inversion and **(b)** validation data sets for the SPiRaL starting model in the period band 50-100 seconds.

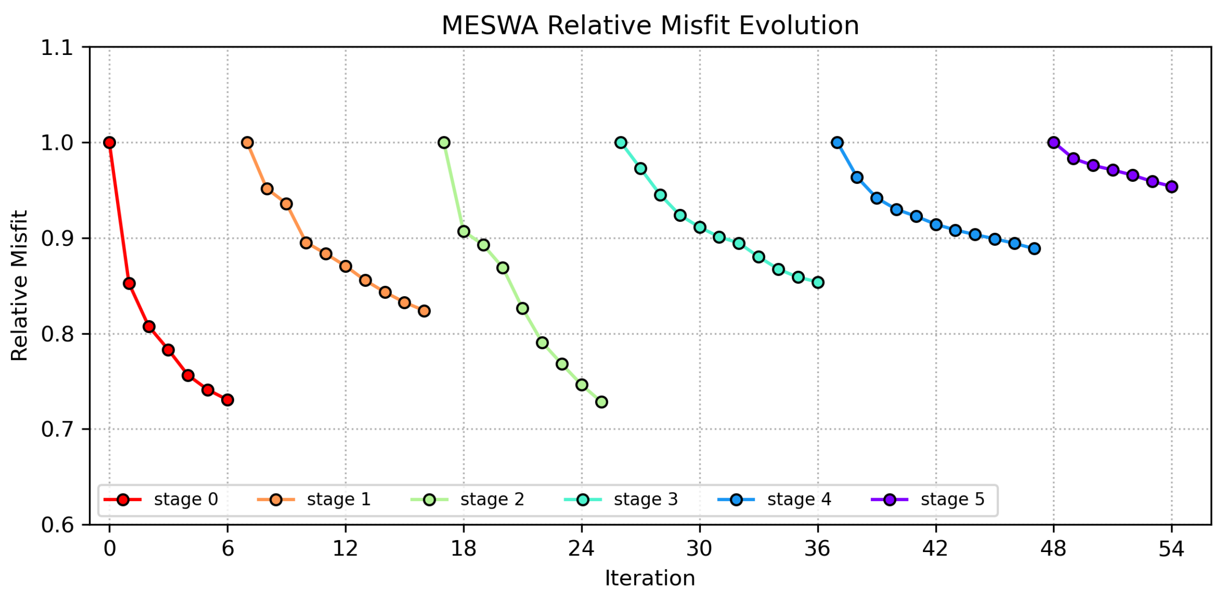

Figure 6. Misfit evolution as a function of iteration number for the relative misfit reduction within each inversion stage (colored symbols).

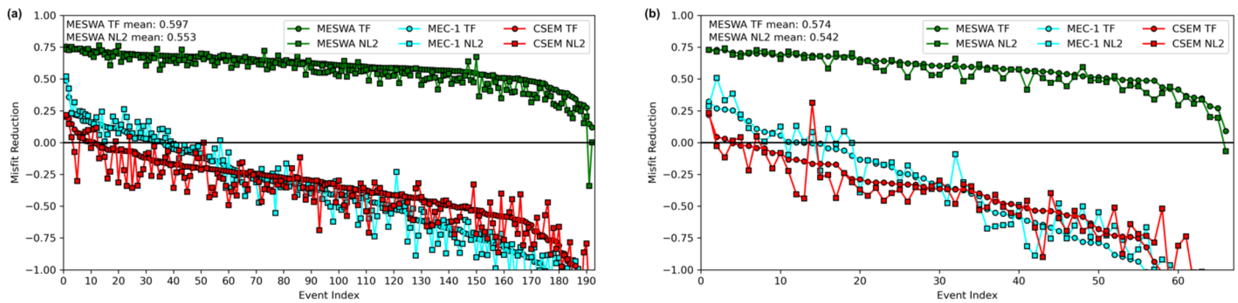

Figure 7. Event-averaged time-frequency phase (TF) and normalized L2 (NL2) misfit reductions for our final MESWA model (green) relative to the SPiRaL starting model for the **(a)** inversion data set and **(b)** validation data set. Also shown are the misfit reductions for the MEC-1 (cyan) and CSEM (red) models. Events are sorted by misfit reduction highest-to-lowest for the MESWA model and the mean TF and NL2 reductions for MESWA are recorded in text on each panel.

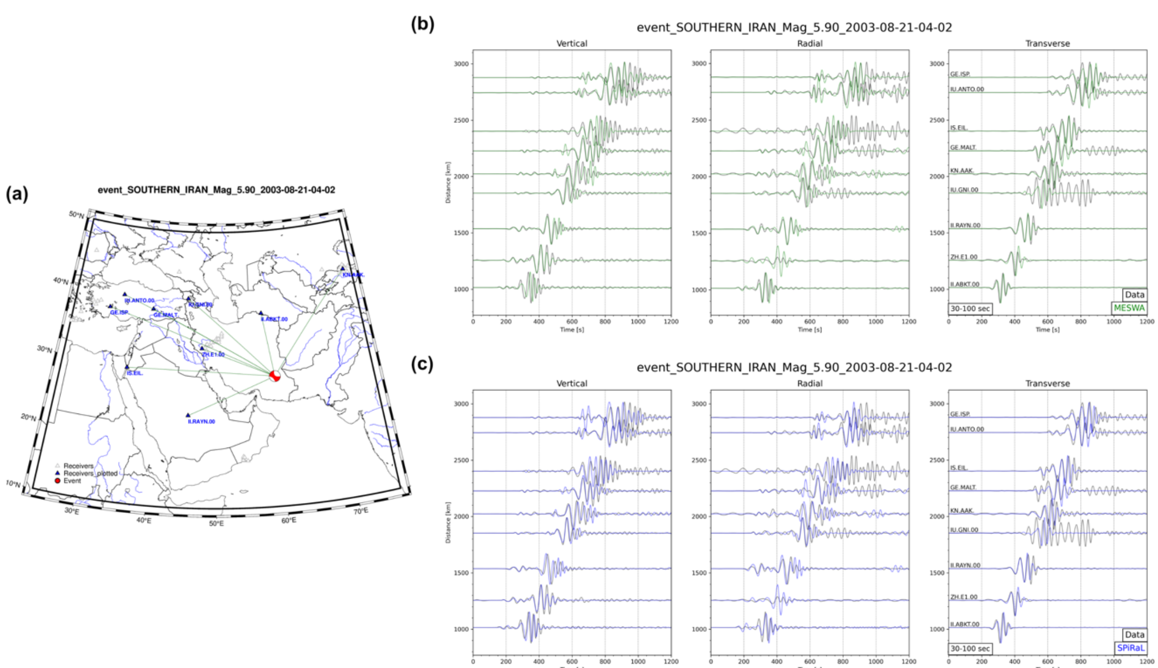

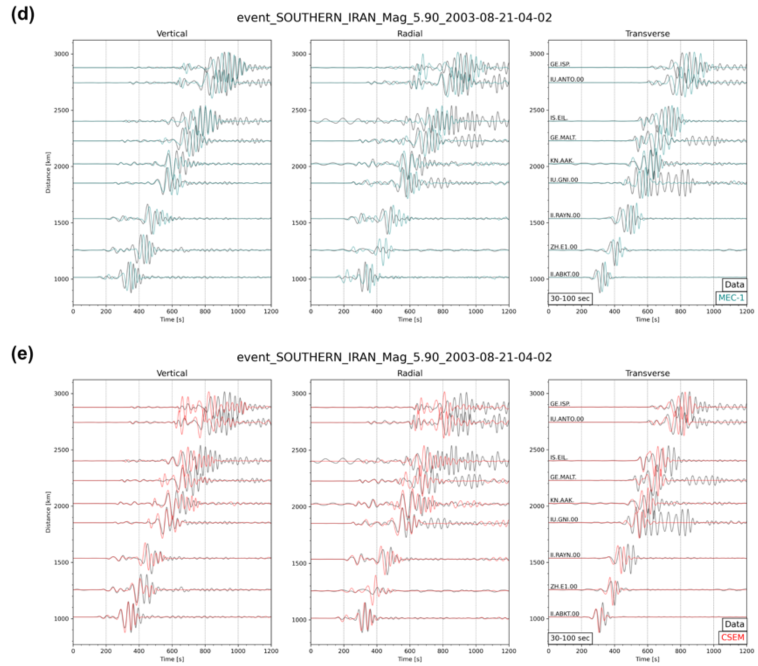

Figure 8. Examples of waveform fits for an M_W 5.90 earthquake in Southern Iran (date: 2003-08-21). **(a)** Map of the event (moment tensor) and stations (blue triangles) for which waveforms are shown. Three-component (vertical, radial and transverse) observed (black) and synthetic (colored) waveforms filtered 30-100 seconds for four models: **(b)** MESWA (green); **(c)** SPiRaL (blue); **(d)** MEC-1 (teal) and **(e)** CSEM (red).

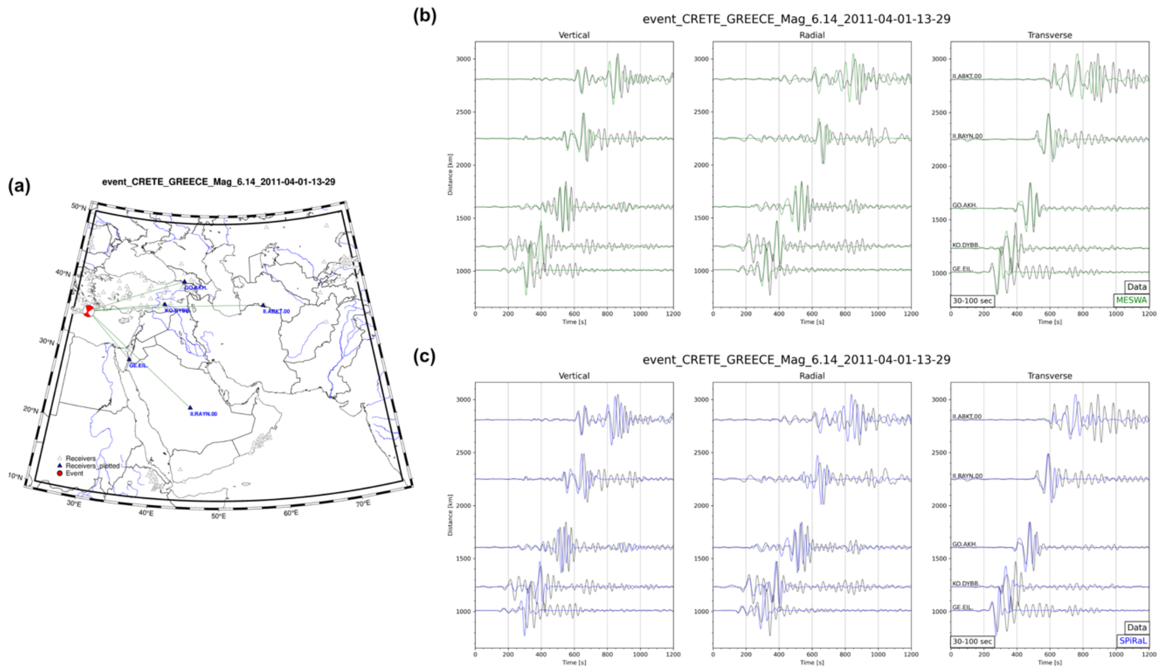

Figure 9. Examples of waveform fits for an M_W 6.14 event in Crete, Greece (date: 2011-04-01). **(a)** Map of the event (moment tensor) and stations (blue triangles) for which waveforms are shown. Three-component (vertical, radial and transverse) observed (black) and synthetic (colored) waveforms filtered 30-100 seconds for two models: **(b)** MESWA (green) and **(c)** SPiRaL (blue).

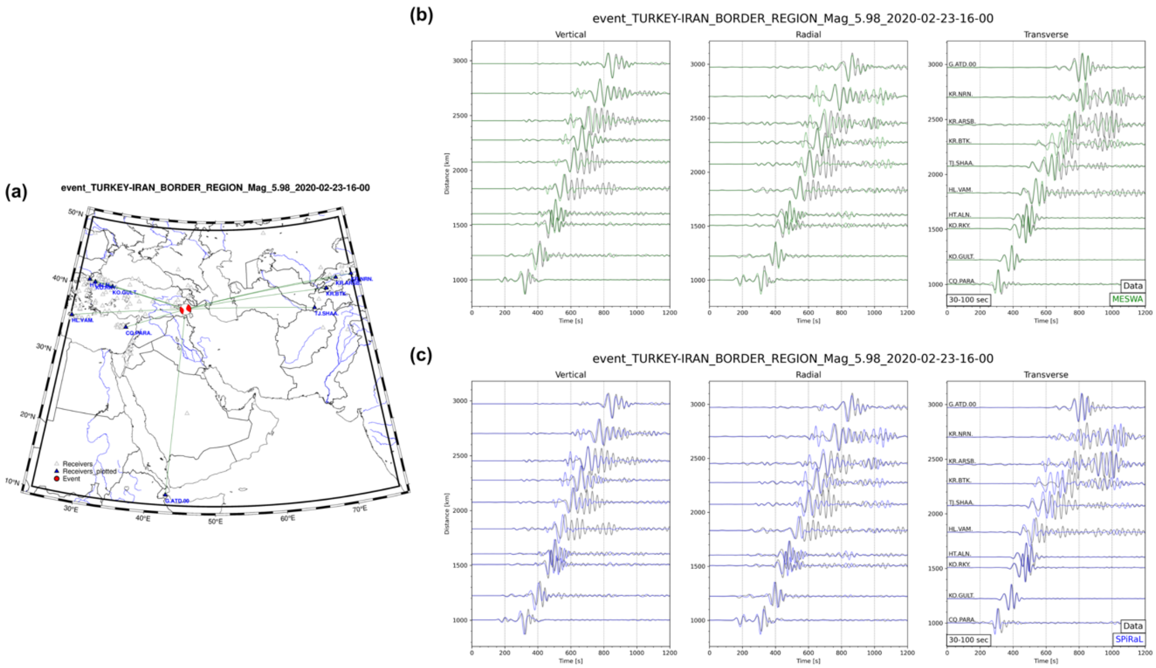

Figure 10. Examples of waveform fits for an M_W 5.98 event on the Turkey-Iran border region (date: 2020-02-23). **(a)** Map of the event (moment tensor) and stations (blue triangles) for which waveforms are shown. Three-component (vertical, radial and transverse) observed (black) and synthetic (colored) waveforms filtered 30-100 seconds for two models: **(b)** MESWA (green) and **(c)** SPiRaL (blue).

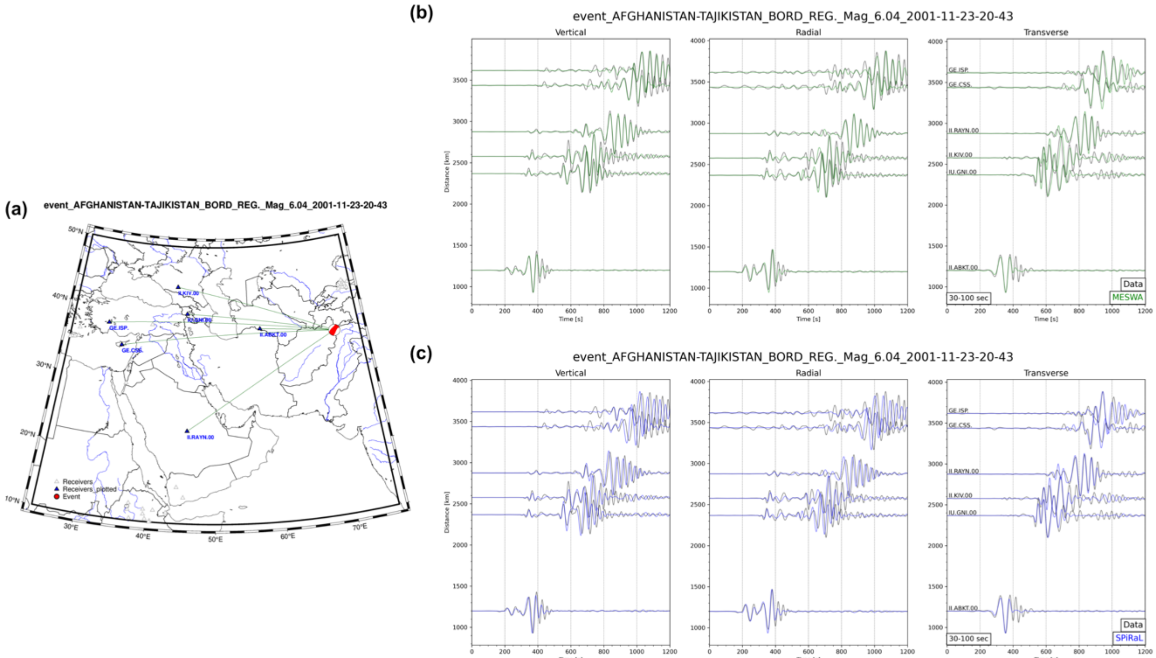

Figure 11. Examples of waveform fits for an M_W 6.04 Afghanistan-Tajikistan border region (date: 2001-11-23). **(a)** Map of the event (moment tensor) and stations (blue triangles) for which waveforms are shown. Three-component (vertical, radial and transverse) observed (black) and synthetic (colored) waveforms filtered 30-100 seconds for two models: **(b)** MESWA (green) and **(c)** SPiRaL (blue).

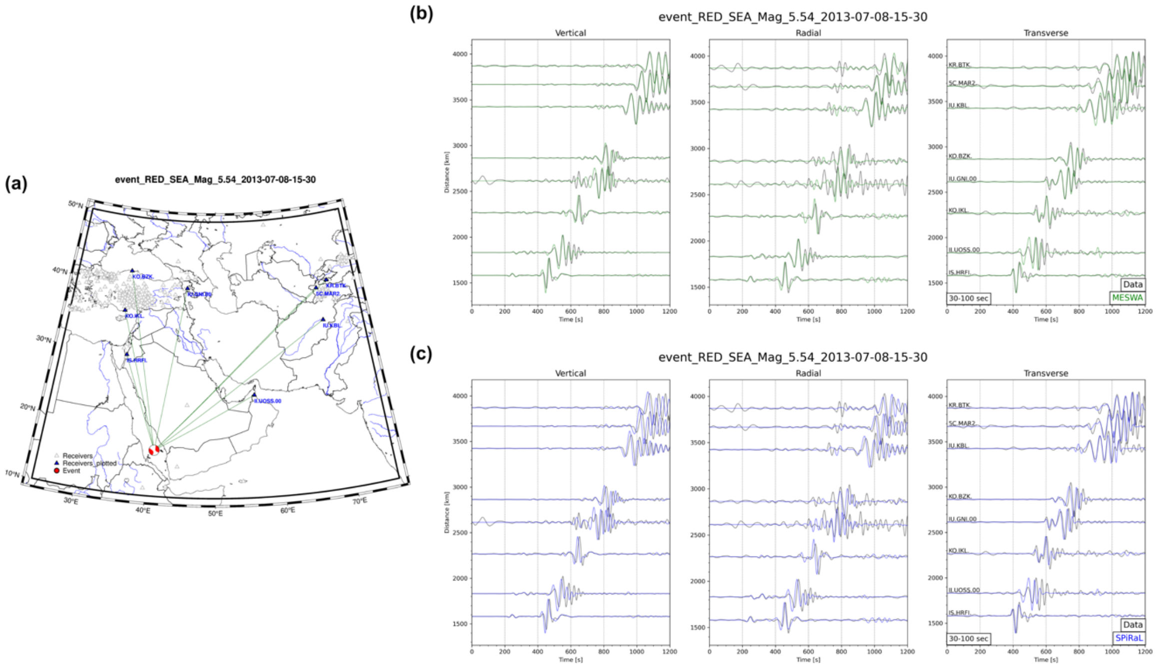

Figure 12. Examples of waveform fits for an M_W 5.54 Red Sea (date: 2013-07-08). **(a)** Map of the event (moment tensor) and stations (blue triangles) for which waveforms are shown. Three-component (vertical, radial and transverse) observed (black) and synthetic (colored) waveforms filtered 30-100 seconds for two models: **(b)** MESWA (green) and **(c)** SPiRaL (blue).

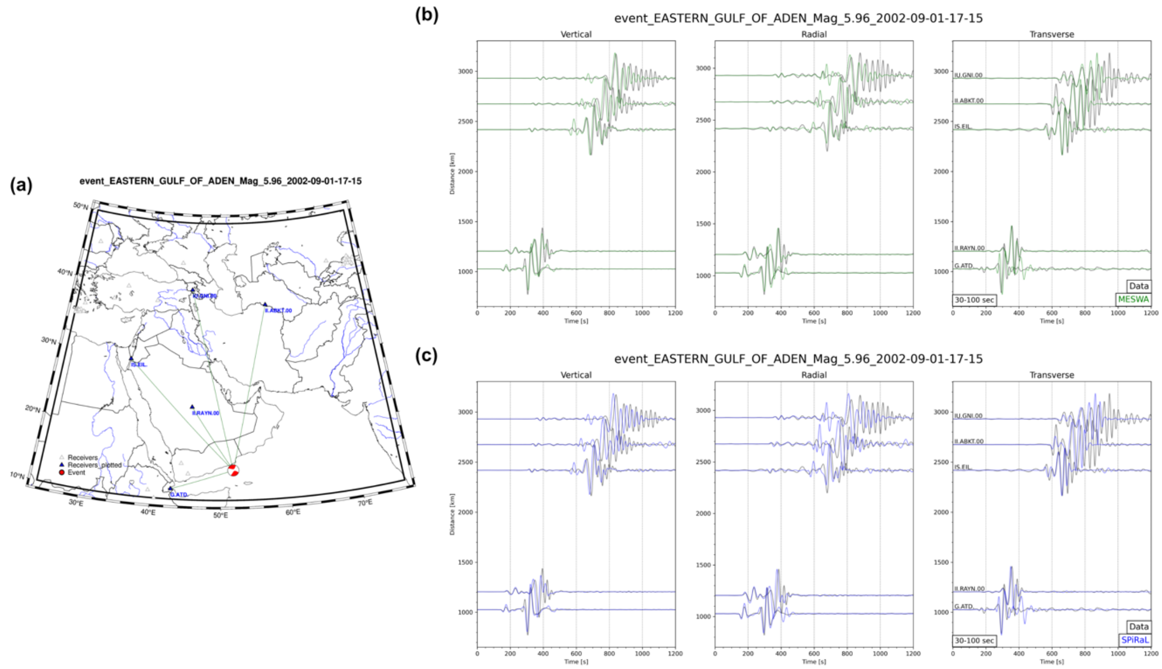

Figure 13. Examples of waveform fits for an M_W 5.96 Eastern Gulf of Aden (date: 2002-09-01). **(a)** Map of the event (moment tensor) and stations (blue triangles) for which waveforms are shown. Three-component (vertical, radial and transverse) observed (black) and synthetic (colored) waveforms filtered 30-100 seconds for two models: **(b)** MESWA (green) and **(c)** SPiRaL (blue).

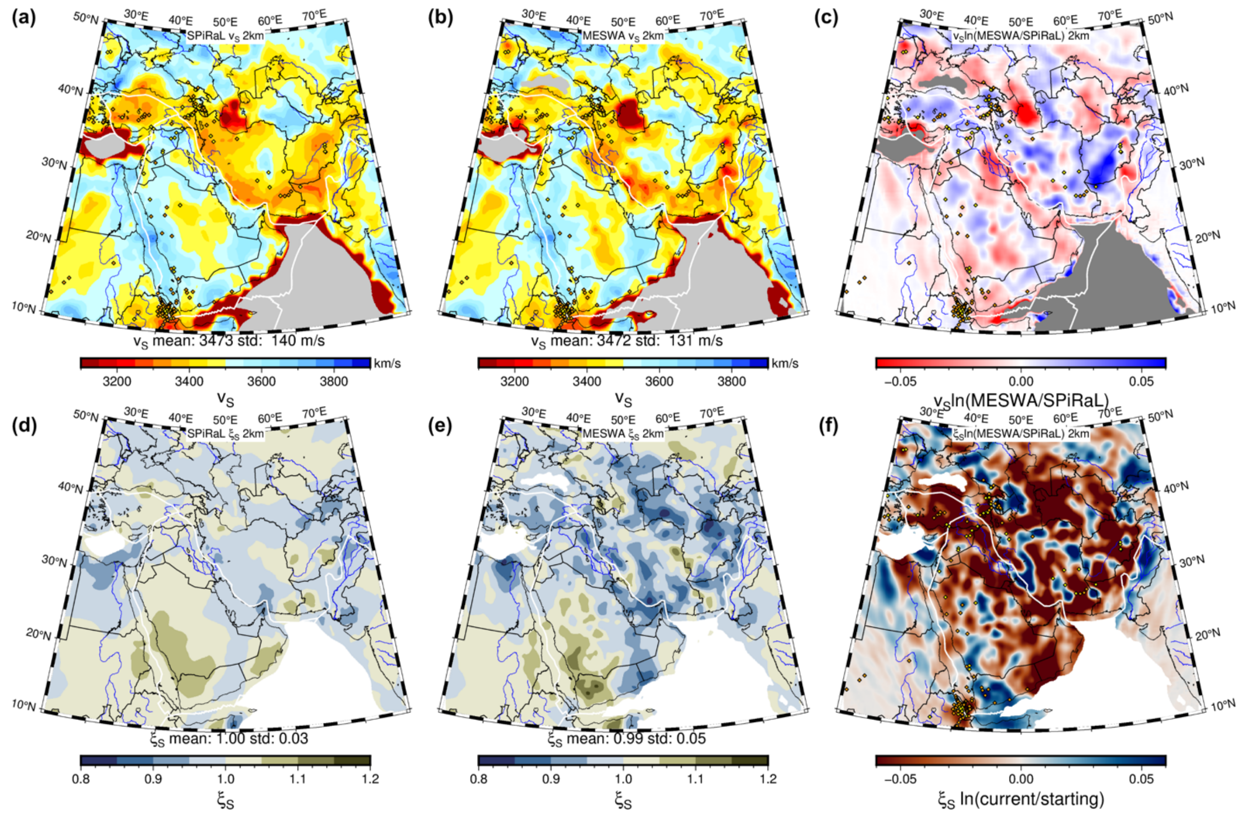

Figure 14. Map of the isotropic shear wavespeeds, v_S, at depth of 2 km below sea level for **(a)** the SPiRaL (Simmons et al., 2021) starting model and the **(b)** MESWA with **(c)** the natural logarithm ratio of v_S (MESWA/SPiRaL). Also shown are maps of the anisotropy parameter, ξ_S, in the same fashion: **(d)** SPiRaL starting model; **(e)** MESWA and **(f)** the natural logarithm ratio of ξ_S (MESWA/SPiRaL). Also shown are volcanic centers and Makran slab contour (Figure 1).

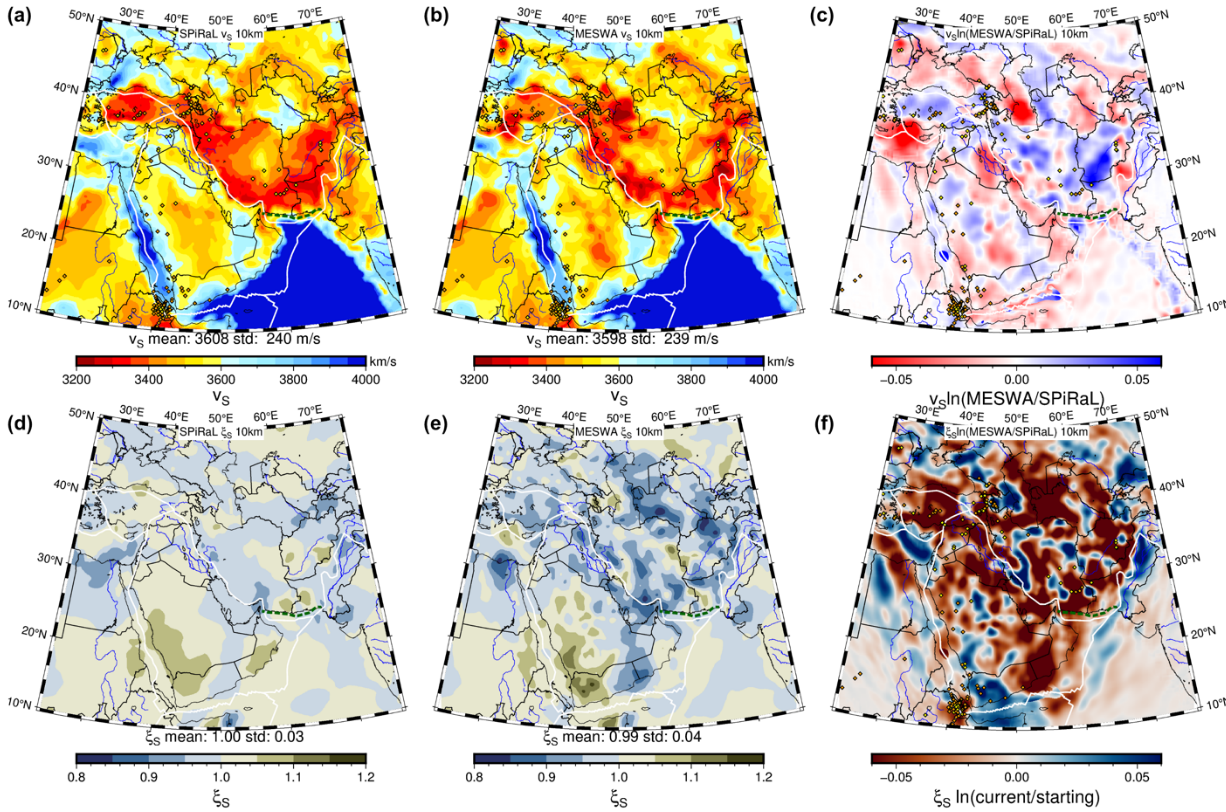

Figure 15. Same as Figure 14, but for a depth of 10 km.

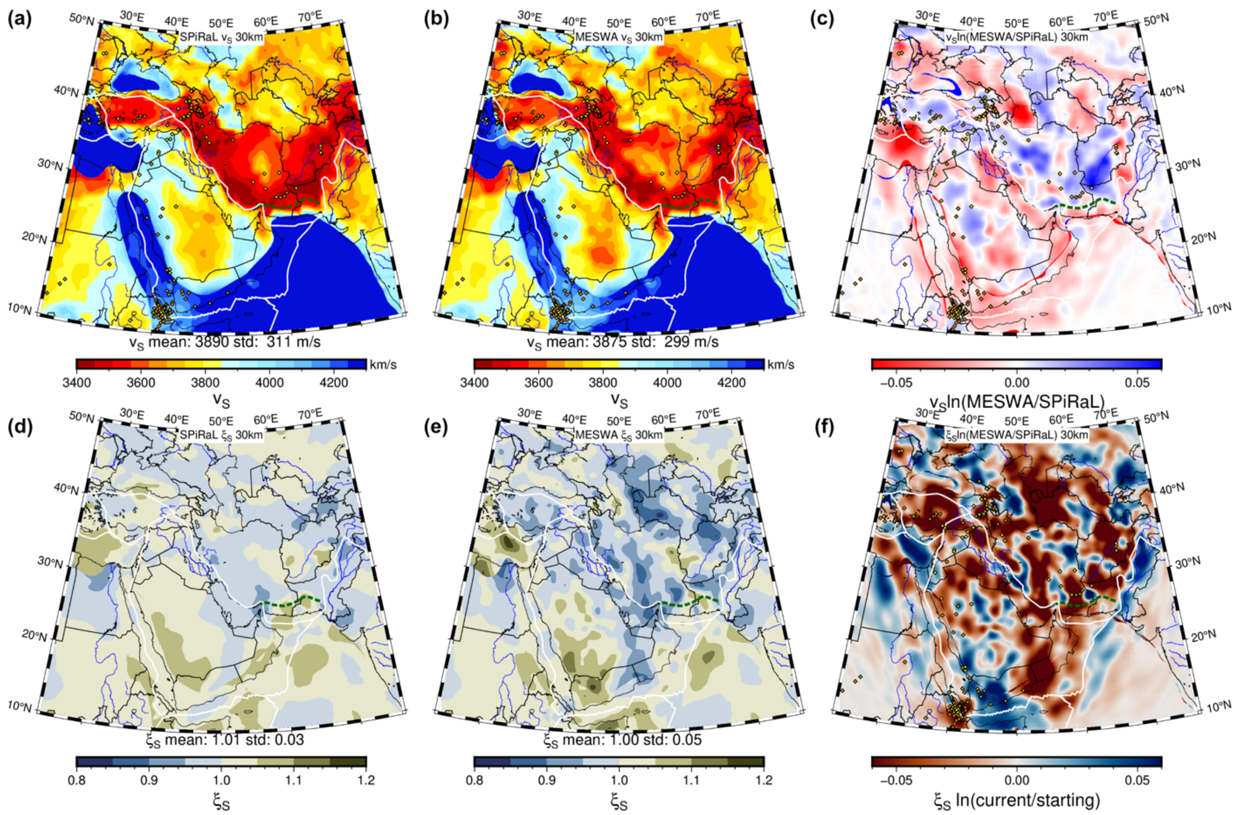

Figure 16. Same as Figure 14, but for a depth of 30 km.

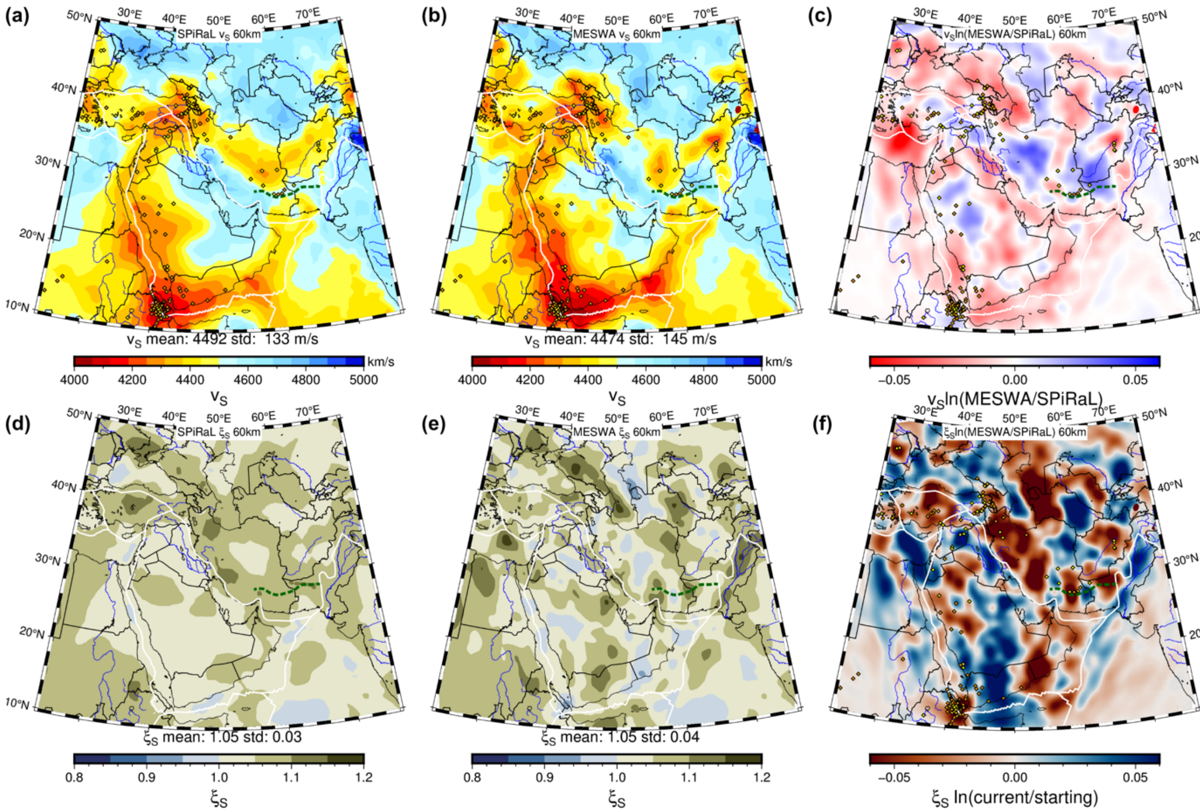

Figure 17. Same as Figure 14, but for a depth of 60 km.

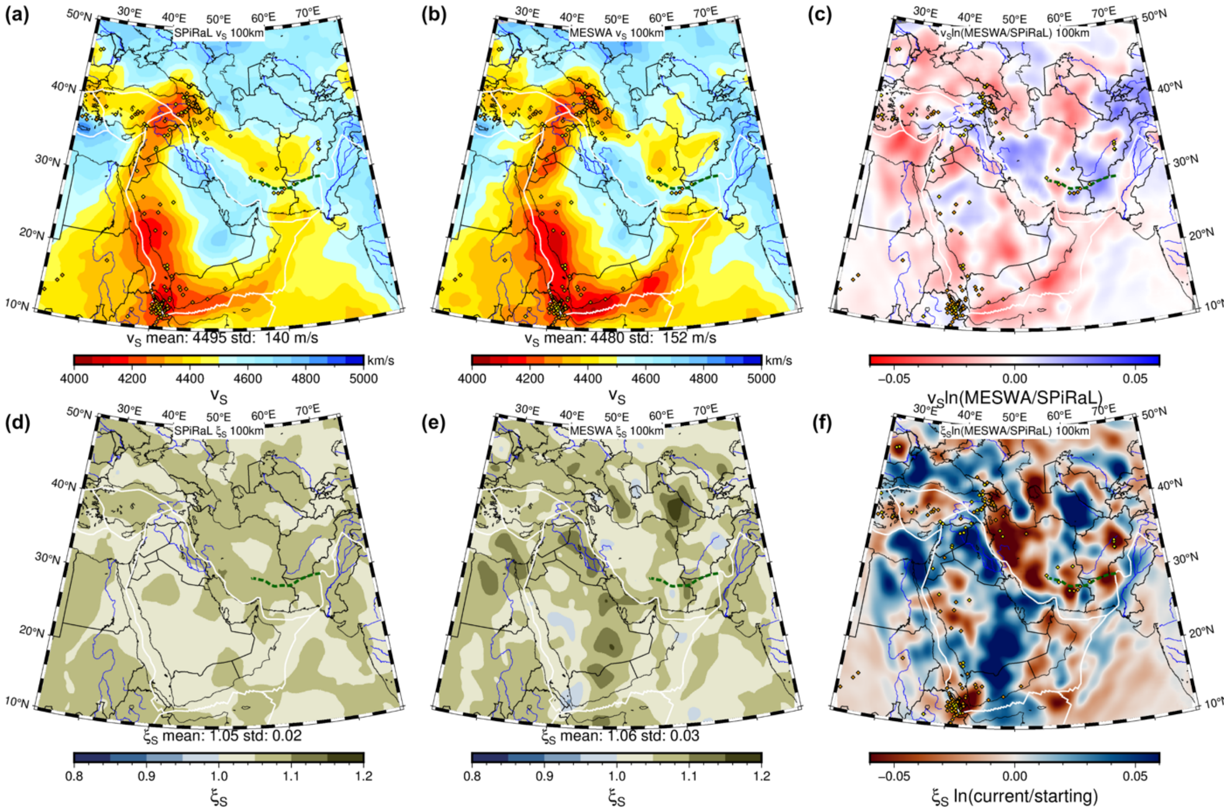

Figure 18. Same as Figure 14, but for a depth of 100 km.

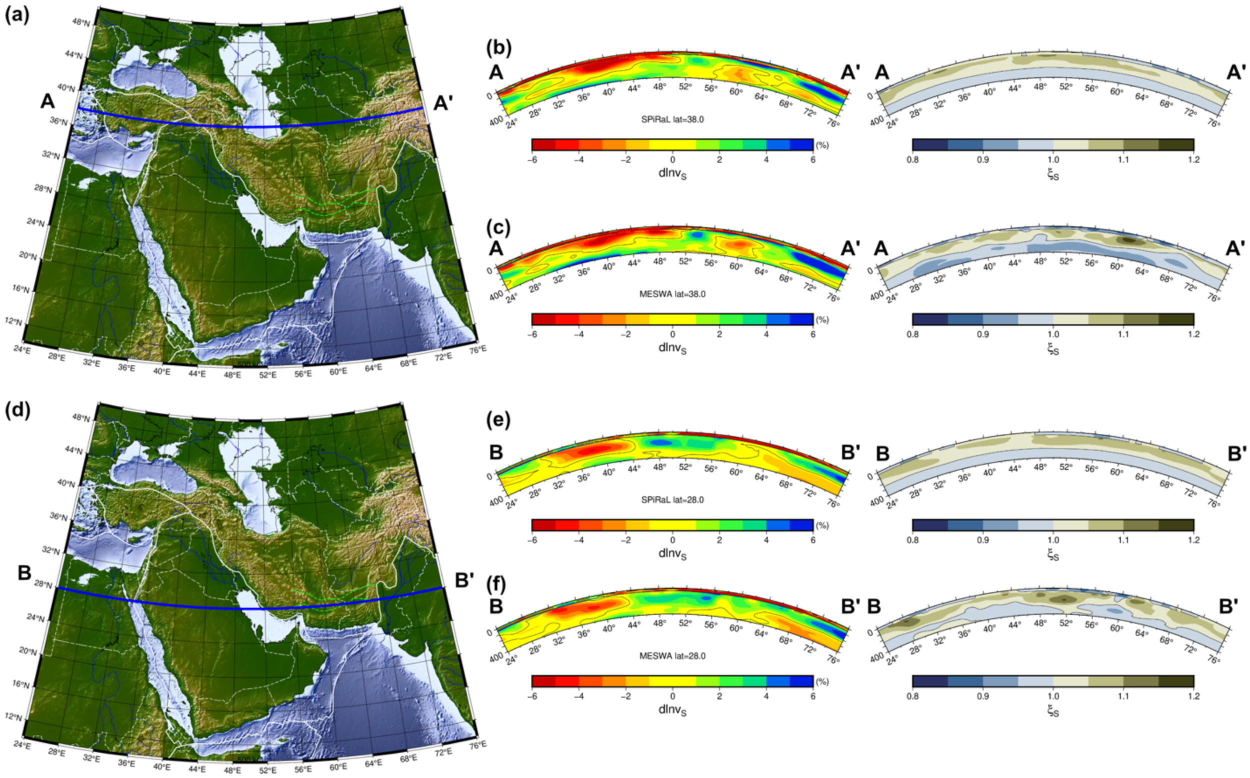

Figure 19. West-east cross-sections: **(a)** map of section A-A'; **(b)** v_S and ξ_S for the SPiRaL starting model along A-A'; **(c)** v_S and ξ_S for the MESWA model along A-A'; **(d)** map of section B-B'; **(e)** v_S and ξ_S for the SPiRaL starting model along B-B'; **(f)** v_S and ξ_S for the MESWA model along B-B'.

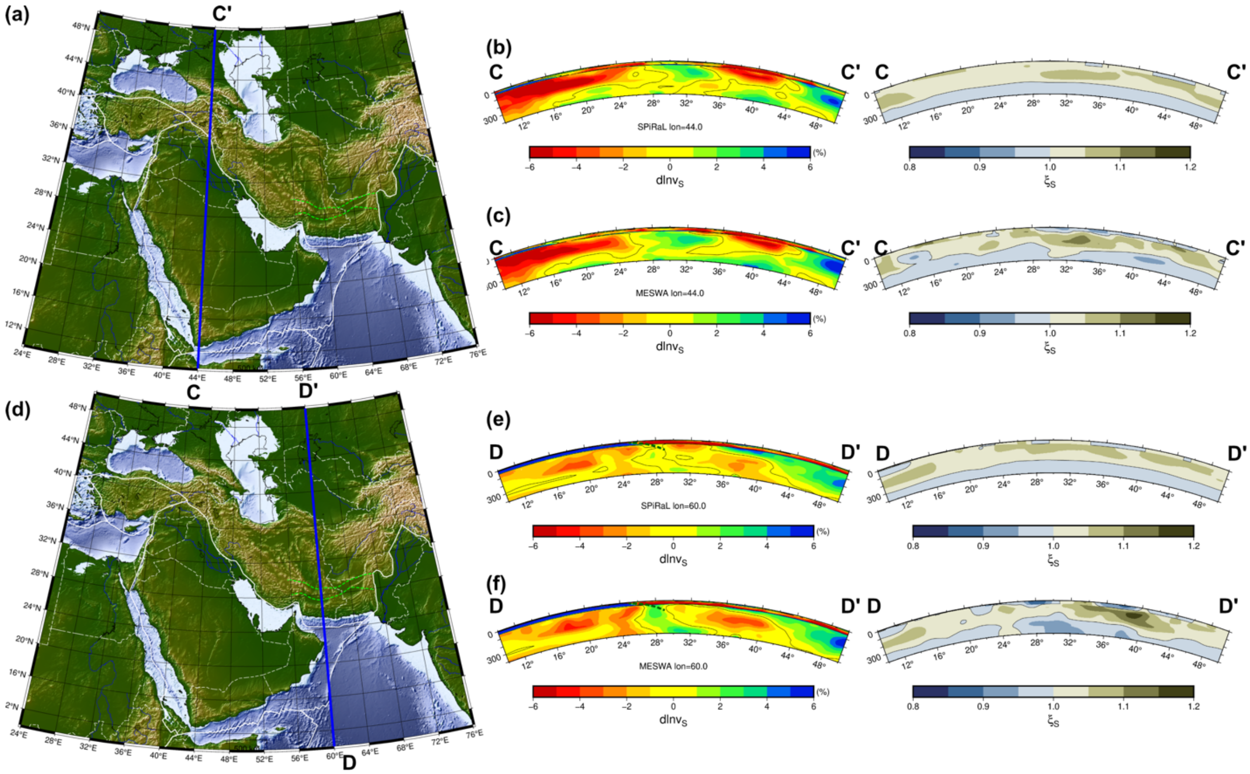

Figure 20. South-north cross-sections: **(a)** map of section C-C'; **(b)** v_S and ξ_S for the SPiRaL starting model along C-C'; **(c)** v_S and ξ_S for the MESWA model along D-D'; **(d)** map of section D-D'; **(e)** v_S and ξ_S for the SPiRaL starting model along D-D'; **(f)** v_S and ξ_S for the MESWA model along B-B'.